# Intergalactic stars in $z \sim 0.25$ galaxy clusters: systematic properties from stacking of Sloan Digital Sky Survey imaging data

Stefano Zibetti,[1,2]⋆ Simon D. M. White,[1] Donald P. Schneider[3] and Jon Brinkmann[4]

[1]*Max-Planck-Institut für Astrophysik, Karl-Schwarzschild-Str. 1, D-85748 Garching bei München, Germany*
[2]*Max-Planck-Institut für Extraterrestrische Physik, Giessenbachstrasse, D-85748 Garching bei München, Germany*
[3]*Department of Astronomy and Astrophysics, Pennsylvania State University, University Park, PA 16802, USA*
[4]*Apache Point Observatory, PO Box 59, Sunspot, NM 88349, USA*

**ABSTRACT**

We analyse the spatial distribution and colour of the intracluster light (ICL) in 683 clusters of galaxies between $z = 0.2$ and 0.3, selected from $\sim$1500 deg$^2$ of the first data release of the Sloan Digital Sky Survey (SDSS-DR1). Surface photometry in the $g$-, $r$- and $i$-bands is conducted on stacked images of the clusters, after rescaling them to the same metric size and masking out resolved sources. We are able to trace the average surface brightness (SB) profile of the ICL out to 700 kpc, where it is less than $10^{-4}$ of the mean surface brightness of the dark night sky. The ICL appears as a clear surface brightness excess with respect to an inner $R^{1/4}$ profile which characterizes the mean profile of the brightest cluster galaxies (BCGs). The surface brightness of the ICL ranges from 27.5 mag arcsec$^{-2}$ at 100 kpc to $\sim$32 mag arcsec$^{-2}$ at 700 kpc in the observed $r$-band. This corresponds to a value of SB in the range 26.5–31 in the rest-frame $g$-band. We find that, on average, the ICL contributes only a small fraction of the total optical emission in a cluster. Within a fixed metric aperture of 500 kpc, this fraction is $10.9 \pm 5.0$ per cent for our clusters. A further $21.9 \pm 3.0$ per cent is contributed on average by the BCG itself. The radial distribution of the ICL is more centrally concentrated than that of the cluster galaxies, but the colours of the two components are identical within the statistical uncertainties. In the mean the ICL is aligned with and *more flattened* than the BCG itself. This alignment is substantially stronger than that of the cluster light as a whole. We find the surface brightness of the ICL to correlate both with BCG luminosity and with cluster richness, while the fraction of the total light in the ICL is almost independent of these quantities. These results support the idea that the ICL is produced by stripping and disruption of galaxies as they pass through the central regions of clusters. Our measurements of the diffuse light also constrain the faint-end slope of the cluster luminosity function. Slopes $\alpha < -1.35$ would imply more light from undetected galaxies than is observed in the diffuse component.

**Key words:** galaxies: clusters: general – galaxies: elliptical and lenticular, cD – galaxies: evolution – galaxies: formation – galaxies: interactions – diffuse radiation.

## 1 INTRODUCTION

First proposed by Zwicky (1951), the presence of a diffuse population of intergalactic stars in galaxy clusters is now a well-established observational fact. After pioneering work in the 1970s based on photographic plates (e.g. Welch & Sastry 1971) and photoelectric detectors (Melnick, Hoessel & White 1977), CCD detectors have made it possible to conduct deep surveys in nearby galaxy clusters and to detect unambiguously the intracluster light (ICL) (e.g.

Bernstein et al. 1995; Gonzalez et al. 2000; Feldmeier et al. 2002, 2004b; Gonzalez, Zabludoff & Zaritsky 2005). Parallel searches for resolved intracluster stars (Durrell et al. 2002) and planetary nebulae (e.g. Arnaboldi et al. 1996; Feldmeier et al. 2004c) have confirmed the presence of a population of stars which are not dynamically bound to any individual galaxy, but orbit freely in the cluster potential. The ICL contributes a substantial fraction of the optical emission in a cluster. Estimates range from approximately 50 per cent in the core of the Coma cluster (Bernstein et al. 1995, although an upper limit of 25 per cent was found over a larger region by Melnick et al. 1977), to 10–20 per cent in less massive clusters (Feldmeier et al. 2004b). Arclets and other morphologically

⋆E-mail: szibetti@mpe.mpg.de

similar low surface brightness features have been identified by several authors in the Coma and Centaurus clusters (Gregg & West 1998; Trentham & Mobasher 1998; Calcáneo-Roldán et al. 2000), suggesting that at least part of the ICL is contributed by dynamically young tidal features. This supports the commonly accepted idea that this stellar population is made up of disrupted dwarf galaxies and of stars stripped from more massive galaxies.

We are still far from having a complete understanding of the physical mechanisms that produce the ICL. Several mechanisms can act to remove stars from individual galaxies and to fling them into intergalactic space. The relative importance and effectiveness of these mechanisms can vary during the evolutionary history of a cluster and from place to place within the cluster. Tides generated by the cluster potential (Merritt 1984) and repeated high-speed encounters between galaxies (Richstone 1976) are the dominant stripping mechanisms in a fixed cluster potential, as demonstrated graphically by the simulations of Moore et al. (1996). However, when the evolution of the cluster and the presence of substructures is taken into account, two other mechanisms become relevant (Gnedin 2003). Preprocessing of the ICL occurs during low-velocity encounters between galaxies within the groups which eventually merge into the cluster, and galaxies are dynamically heated by encounters with substructures. As stressed by Mihos (2004), the tidal tails and the heated structures preprocessed within groups are subsequently easily removed by the cluster potential.

In order to encompass all these processes in a cosmologically motivated framework, many groups in recent years have addressed the ICL problem using high-resolution $N$-body simulations (Napolitano et al. 2003), some including smoothed particle hydrodynamics (SPH) to take gas processes into account (Murante et al. 2004; Willman et al. 2004; Sommer-Larsen, Romeo & Portinari 2005). Although many issues still have to be clarified and agreement between the different models is far from complete, these simulations show how the ICL may be produced over the entire history of the clusters from continuous stripping of member galaxies and through contributions from merging groups. Unfortunately the degree to which they correctly represent the internal structure of cluster galaxies and their dark matter haloes is too uncertain for their prediction for the amount of ICL to be reliable.

Although the number of observations of the ICL in individual clusters has increased rapidly in recent years, we still lack a large sample that allows generalization of the properties of the ICL and an understanding of how they depend on global cluster properties, particularly on richness and on the luminosity of the first ranked galaxy. Given the very low surface brightness of the ICL, typically less than 0.1 per cent of that of the night sky, observations are extremely challenging. Not only are long exposure times required in order to obtain acceptable signal-to-noise (S/N) ratios, but many subtle instrumental effects, such as flat-fielding inhomogeneities and scattered light within the camera, must be kept under tight control.

An alternative approach, which exploits the wealth of imaging data made available by the Sloan Digital Sky Survey (SDSS, York et al. 2000), has been proposed and successfully applied to the study of stellar haloes around galaxies by Zibetti, White & Brinkmann (2004). By stacking several hundred images, mean surface brightnesses of the order of $\mu_r = 29$–$30$ mag arcsec$^{-2}$ can be reliably measured. In fact, not only is the S/N enhanced, but also inhomogeneities in the background signal and in flat fielding are averaged out. A further advantage comes from the fact that the SDSS images are obtained in drift-scan mode (Gunn et al. 1998). As opposed to the 'staring' mode, in which the intensity of each pixel in the image is measured by the corresponding pixel on the CCD array, in drift-scan mode the signal is integrated over an entire column of the CCD while the target drifts in the field of view. Therefore, sensitivity variations can occur only in one dimension (i.e. perpendicular to the drift direction) instead of two; this strongly reduces the flat-field inhomogeneities in the frames.

The stacking analysis is statistical in its nature, providing mean results for large samples of galaxy clusters, which can be compared in principle to similar properties derived from cosmological simulations. An appropriate choice of subsamples makes it possible to study the influence of different parameters on the properties of the ICL. Although high statistical significance is the main advantage of the stacking method, individual features (tidal streams and arclets, for instance) and real cluster-to-cluster variations are lost in the averaging. The stacking method is therefore complementary to imaging of individual clusters, from which detailed information about small-scale structures and stochastic phenomena can be derived.

In this paper we present an analysis of the stacking of 683 clusters imaged in the $g$-, $r$-, and $i$-bands in the SDSS. They were selected over $\sim1500$ deg$^2$ between $z = 0.2$ and 0.3, using the maxBCG method (Annis et al., in preparation). Details on the sample selection and on sample properties are given in Section 2. The image processing and the stacking technique are described in Section 3. In Section 4 we describe how the relevant photometric quantities are derived. We present the results of our analysis in Section 5. Possible sources of systematic uncertainties on the derived quantities are discussed in Section 6. Our results are compared to other extant observations and model predictions in Section 7, and some possible implications for theories of the formation of the ICL during cluster evolution are presented. Conclusions and future perspectives are outlined in Section 8.

Throughout the paper we adopt the 'concordance' cosmology, $H_0 = 70$ km sec$^{-1}$ Mpc$^{-1}$, $\Omega_0 = 1$, $\Omega_\Lambda = 0.7$.

## 2 THE SAMPLE

The imaging data utilized in this work are derived from the SDSS (York et al. 2000; Stoughton et al. 2002; Abazajian et al. 2003, 2004). The SDSS is imaging about a quarter of the sky in the $u$-, $g$-, $r$-, $i$- and $z$-bands, with a $\sim54$-s exposure in drift-scan mode at the dedicated 2.5-m Apache Point Observatory telescope (Fukugita et al. 1996; Gunn et al. 1998; Hogg et al. 2001; Smith et al. 2002; Pier et al. 2003), reaching $\sim25$ mag arcsec$^{-2}$ at S/N $\sim1$ for a single pixel in the $r$-band. The SDSS spectroscopic galaxy samples (Blanton et al. 2003a) consist of all galaxies brighter than $r = 17.77$ mag (Strauss et al. 2002) and of a sample of luminous red galaxies (Eisenstein et al. 2001) extending at $r < 19.2$ mag.

To reach surface brightnesses as low as 29–30 mag arcsec$^{-2}$ stacking of several hundreds of images is required. We have focused our sample selection on clusters in the redshift range 0.2–0.3 in order to satisfy the requirement of homogenous imaging coverage within each cluster. Along the scan direction the main limitation is given by the sky background fluctuations, whereas in the perpendicular direction the limit is given by the width of the SDSS camera columns (Gunn et al. 1998), which corresponds to $\sim13.5$ arcmin. For practical convenience we use only the SDSS fpC frame (13.5 $\times$ 9.8 arcmin$^2$) in which the cluster centre is located and require that a significant fraction of 'background' beyond 1 Mpc projected distance from the cluster centre be included. Given that 1 Mpc = 5.05 arcmin at $z = 0.2$, this turns out to be a good lower redshift limit. On the other hand, we prefer to avoid extending the sample to much higher redshift, both because cosmological dimming acts to reduce the apparent surface brightness by $(1 + z)^4$, and because

resolving individual galaxies in the clusters becomes increasingly difficult. Moreover, *K*-corrections for band shifting would have to be taken into account in order to interpret a stack of objects in a wide range of *z*. Since we do not know a priori the spectral energy distribution (SED) of the ICL, this would add considerable uncertainty to our results. The 4000-Å break is probably the main feature in the SED of the ICL, so we have chosen $z = 0.3$ as an upper limit; the break is then almost homogeneously bracketed by the $g - r$ colour over the whole sample.

Cluster identifications over an area of ∼1500 deg² in the SDSS-DR1 (Abazajian et al. 2003) have been kindly provided by J. Annis, based on the maxBCG method (see Annis et al., in preparation, Bahcall et al. 2003, for details). This method is based on the fact that (i) the brightest cluster galaxies (BCGs) lie in a narrow region of the $(g-r) - (r-i) - M_i$ space, and (ii) the early-type galaxies in a cluster define a ridge line in the colour–magnitude diagram. The likelihood of a galaxy being the BCG of a cluster is calculated for a grid of different redshifts taking into account the 'distance' of the galaxy from the predicted BCG locus and the number of galaxies $N_{gal}$ within $1\ h^{-1}$ Mpc which lie less than $2\sigma$ away from the early-type colour–magnitude relation ($\sigma$ being the average scatter of the relation). The redshift which maximizes the likelihood is taken as the fiducial redshift of the cluster; only clusters whose probability is greater than a certain threshold are considered. In addition to the identification of the BCG and the photometric redshift of the cluster, the maxBCG method produces the number of red-sequence galaxies within $1\ h^{-1}$ Mpc, $N_{gal}$, their total luminosity, $L_{RG}$, and the number of red-sequence galaxies within $0.33\ h^{-1}$ Mpc, $N_{gal,3}$. Based on the analysis conducted by Hansen et al. (2002) and Hansen et al. (2005) on the galaxy count overdensity around 12 830 BCGs in the redshift interval $0.07 \leqslant z < 0.3$, an estimate of $R_{200}$[1] is given using the empirical relation found by these authors between $N_{gal}$ and $R_{200}$.

From the maxBCG catalogue we have selected all the clusters with: $0.15 \leqslant z_{maxBCG} \leqslant 0.35$; $N_{gal} \geqslant 15$; $N_{gal,3} \geqslant 5$. This preliminary selection uses a broader redshift range to include those BCGs whose spectroscopic *z* is within the 0.2–0.3 interval, although the maxBCG *z* is not (see below). The constraints on the number of galaxies within 1 and $0.33\ h^{-1}$ Mpc should ensure that we select clusters with richness similar to those listed in the Abell catalogue (Abell 1958; Abell, Corwin & Olowin 1989). The positions of the BCGs that passed this first selection have been matched to objects in the SDSS spectroscopic data base. Whenever available, the spectroscopic redshift of the BCG has been assigned as the fiducial redshift of the entire cluster (see Annis et al., in preparation, for details on the precision achieved by the maxBCG in the redshift determinations). All selected clusters with $0.195 < z < 0.3$ have been inspected using RGB composite images ($g - r - i$) in order: (i) to exclude the images affected by evident defects, such as strong background gradients, and scattered light from very bright stars; (ii) to check that the selected BCG is actually the brightest member (the maxBCG algorithm sometimes selects the second or third ranked member), and, if not, to assign the position of the new BCG; (iii) to exclude candidate clusters where no clear enhancement of the galaxy number density is visible toward the centre. This final step prunes the sample of roughly 10 per cent of poor cluster candidates, with a very low spatial concentration. These are likely just chance superposition of galaxies, rather than physically bound associations. A
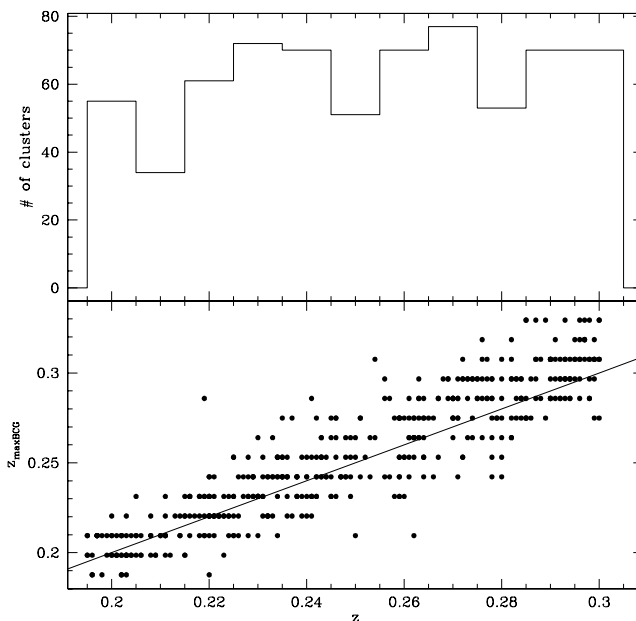


**Figure 1.** The redshift distribution of the galaxy clusters in our main sample (upper panel). In the bottom panel we show the comparison between the spectroscopic (abscissa) and the photometric maxBCG redshifts (ordinates) for the 464 clusters whose BCG has been spectroscopically observed. The $z = z_{maxBCG}$ relation is shown by the straight line.

total of 683 clusters satisfy all these requirements and constitute our main sample.

## 2.1 Sample properties

The distribution in redshift of the main sample is almost uniform between 0.2 and 0.3, as shown in the top panel of Fig. 1, and we will therefore use 0.25 as the reference redshift of the sample. In the bottom panel of the same figure we plot the spectroscopic (in abscissa) and the photometric maxBCG redshifts (in ordinates) for the 464 clusters whose BCG has been spectroscopically observed. The typical error of the photometric redshift is 0.015. Note that 49 of these clusters would have been excluded based on the photometric redshift, as located beyond $z = 0.3$. Considering that among the 219 clusters, for which no spectroscopic redshift is available, only 69 are at $z_{est} > 0.28$, we conclude that fewer than 15–20 clusters of *z* significantly larger than 0.3 contaminate our sample.

The distributions of the other fundamental properties derived from the maxBCG analysis and from the photometry of the BCG are reported in Fig. 2. In the first three panels (a, b and c), we show histograms of the number of clusters as a function of the luminosity of the red-sequence galaxies, of the number of red galaxies, and of the luminosity of the BCG, respectively. The total luminosity and the number of red galaxies are in principle equivalent proxies for the richness of clusters. However, due to the small number of galaxies in the poorest clusters, the luminosity provides a smoother distribution at the poor end. The three distributions are peaked around the average values, with roughly 50 per cent of the sample sharing very similar properties, namely 16–24 red galaxies or $L_{RG} = 15 - 25\ L_{i,-21.0}$,[2] and $m_{r,0.25}$(BCG) between 17.2 and 18. The

---

[1] $R_{200}$ is the radius that encloses an average mass density which is 200 times the density of the background.

[2] $L_{i,-21.0}$ is the luminosity corresponding to $-21.0$ absolute *i*-band mag in the rest frame.
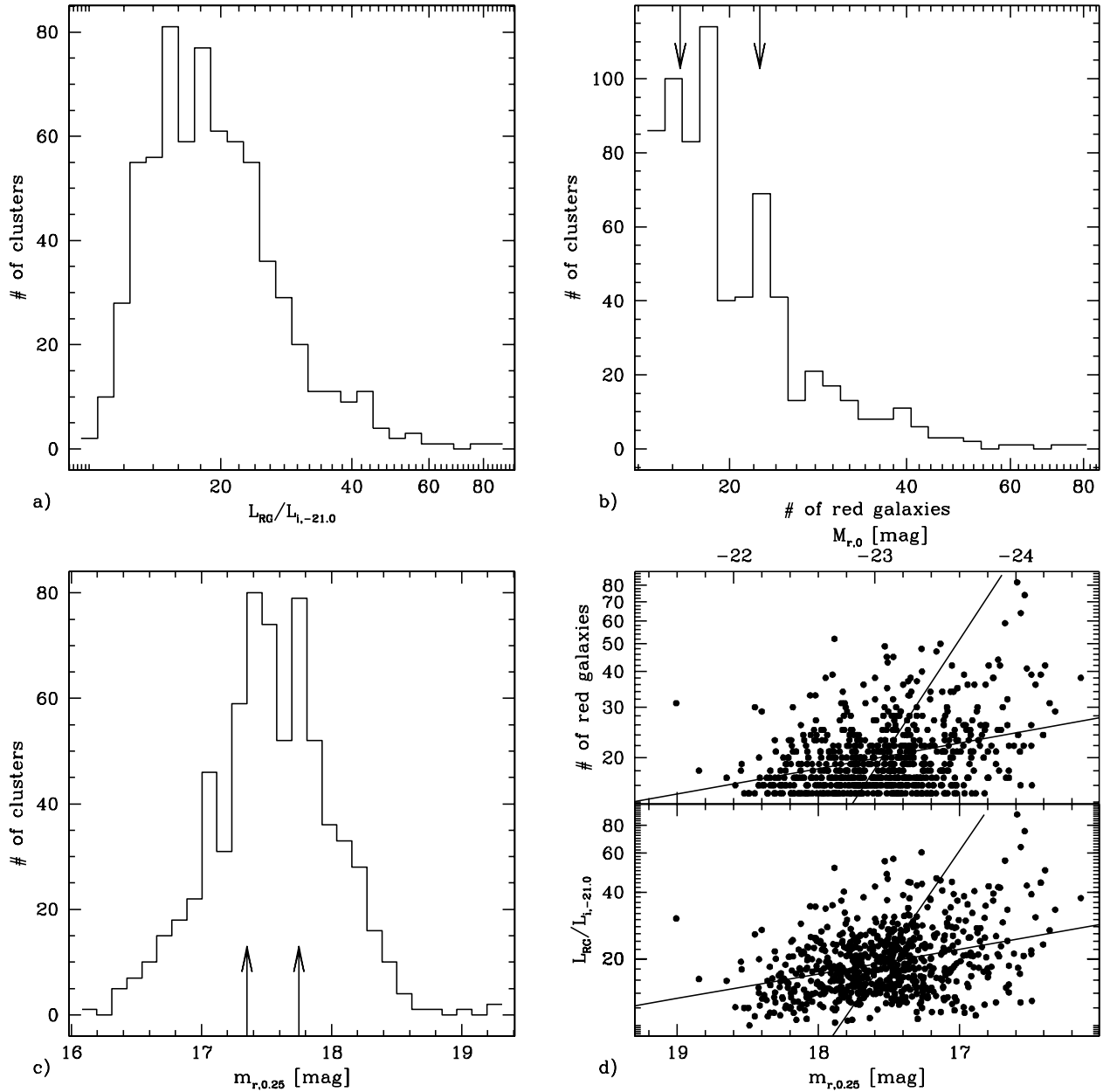
**Figure 2.** Properties of the main sample of galaxy clusters. (a) Distribution of the total luminosity of the red-sequence galaxies. The luminosity is expressed in units of the luminosity corresponding to $M_i = -21.0$. (b) Distribution of the number of red-sequence galaxies. Arrows indicate the upper and lower limits for the 'poor' and 'rich' subsamples respectively. (c) Distribution of BCG luminosities, in units of $r$-mag in the observer frame for $z = 0.25$. Arrows indicate the upper and lower limits for the 'luminous-BCG' and 'faint-BCG' subsamples, respectively. (d) Correlations of the BCG luminosity with the luminosity of the red-sequence galaxies (bottom) and with the number of red-sequence galaxies (top). Solid lines show the direct ($y$ versus $x$) and inverse ($x$ versus $y$) regression lines from the least-squares linear fitting to the points. The scale on the upper axis reports the rest-frame $r$-band absolute magnitudes, using the $K$-corrections calculated for a 13-Gyr old, solar metallicity SSP with the code of Bruzual & Charlot (2003).

well-known correlation between richness and luminosity of the BCG is present in our sample as visible in panel (d). Nevertheless, the scatter is conspicuous and different BCG luminosities can correspond to very different richness.

Unfortunately the redshift range of our sample makes its overlap with the Abell cluster catalogue quite small: although 130 clusters catalogued by Abell et al. (1989) as distance class 6 are included in the area of sky covered by our sample, only 43 match the position of our clusters within 6 arcmin, and have Abell richness ranging from 0 to 4. Most (95 per cent) of the remaining 87 are excluded

because of their low redshift, and just 5 per cent are rejected because of defects in the imaging data.

In Section 5.5 we will analyse the properties of the ICL in different cluster subsamples. In particular we will refer to 'poor' ('P') and 'rich' ('R') clusters as those having less than 17 red galaxies and more than 22,[3] respectively; 'luminous-BCG' ('L') and

---

[3] Note that of the 178 clusters that make up the 'rich' subsample, 31 are catalogued by Abell et al. (1989), corresponding to 17.4 per cent.
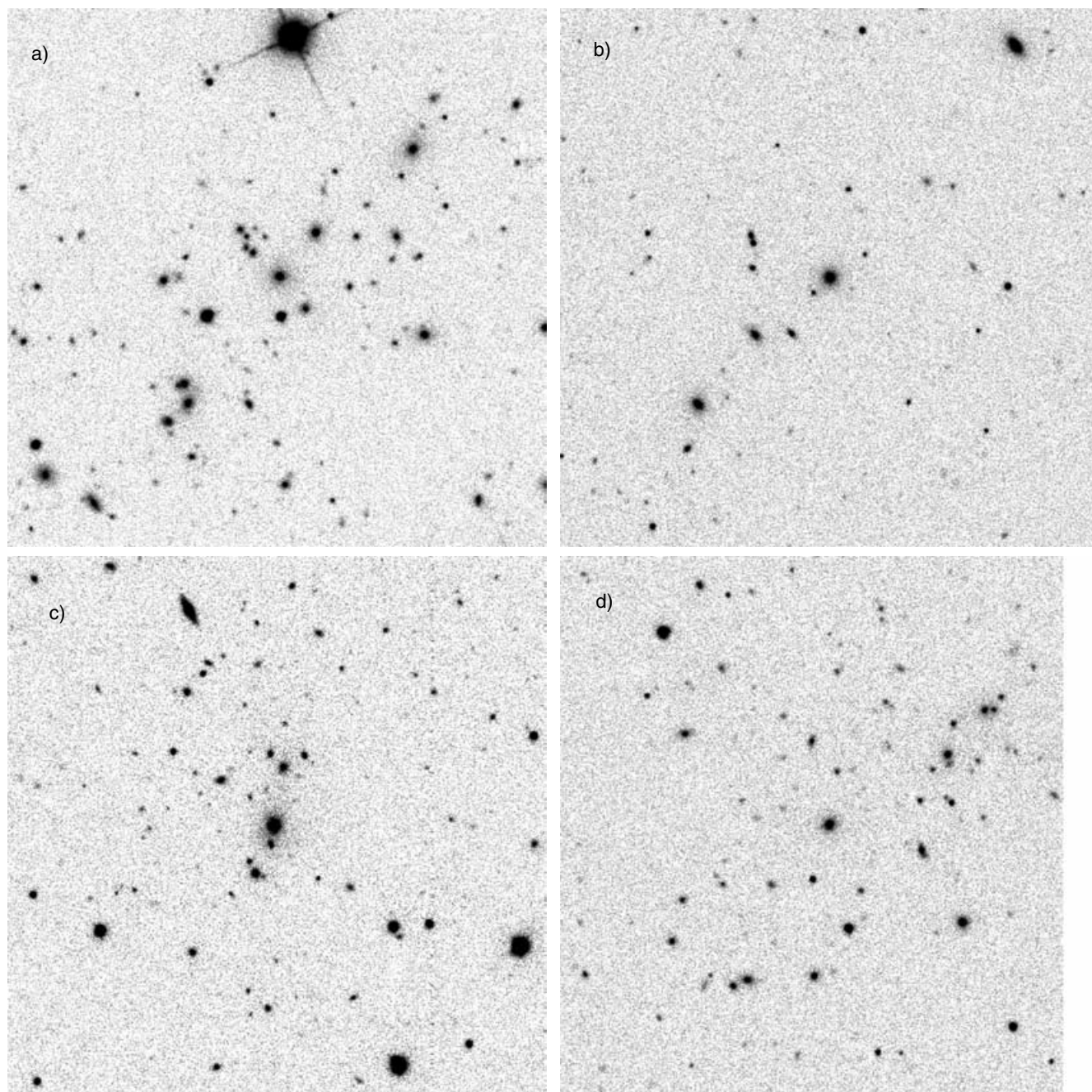
**Figure 3.** *r*-band images of four typical clusters in the 'rich', 'poor', 'luminous-BCG' and 'faint-BCG' subsamples (panels a, b, c and d, respectively). Each frame is 500 × 500 pixel, corresponding to 3.3 arcmin side, ~0.8 $h_{70}^{-1}$ projected Mpc.

'faint-BCG' ('F') clusters are classified according to the luminosity of the BCG, brighter than $m_{r,0.25} = 17.35$ or fainter than 17.75. These boundaries are marked with arrows in panels b and c of Fig. 2. In order to illustrate the differences, we show in Fig. 3 the *r*-band images of four typical clusters in the 'rich', 'poor', 'luminous-BCG' and 'faint-BCG' subsamples (panels a, b, c and d, respectively). It is particularly instructive to see how richness and BCG luminosity do not always correspond, despite their general correlation. Although the BCG of the 'rich' cluster is more luminous than the BCG of the 'faint-BCG' one, it is not significantly brighter than the BCG of the 'poor' cluster. Vice versa, although the 'luminous-BCG' cluster is richer than the 'poor' one, it is not significantly richer than the 'faint-BCG' cluster.

## 3 THE IMAGE PROCESSING AND STACKING

Our stacking technique consists in averaging the images of a large number of galaxy clusters after masking all the unwanted sources. Since we are interested both in the diffuse emission from intracluster stars and in the overall cluster luminosity, including galaxies, two different masks must be utilized. In the first case we mask all the detectable sources excluding the BCG (masks 'A'), while the foreground stellar sources only are masked when studying the total emission (masks 'B'). In this second case, contamination from galaxies not belonging to the clusters is significant. However, thanks to the large number of fields that are stacked, their light is almost uniformly distributed in the stacked frame and their contribution

to the surface brightness can be reliably estimated sufficiently far
from the centre of the cluster. Detection limits and surface bright-
ness thresholds in building the 'A' masks are expected to have an
important influence on the estimated amount of diffuse light: we
will thoroughly discuss this issue in Sections 4.1 and 6.2.

A big advantage of the stacking approach with respect to tradi-
tional imaging of individual clusters resides in the possibility of ap-
plying very conservative masking to the foreground (stellar) sources,
without any significant loss in the measured signal. Combined with
the uniform distribution of contaminating foregrounds in the result-
ing stacked image, this masking makes a careful modelling of the
point spread function (PSF) unnecessary in order to subtract fore-
ground stars.

The SDSS imaging data are available as bias-subtracted, flat-field
corrected frames; adopting the standard SDSS terminology, we will
refer to these as 'corrected frames' in the following. We use only
the three most sensitive SDSS passbands, *g*, *r* and *i*. Before images
can be actually stacked, background subtraction, geometric trans-
formation and intensity rescaling must be applied. For each cluster
we estimate the sky background in an annulus with inner radius cor-
responding to 1 Mpc, 100-kpc thick, centred on the BCG. Sources
lying in that area were masked using the segmentation image ob-
tained by running SEXTRACTOR (Bertin & Arnouts 1996)[4] with a
Gaussian smoothing kernel (FWHM = 4.0 pixel), and a detection
threshold of 0.3 times the local rms and 5 pixel as minimum area.

We extract $1600 \times 1600$ pixel ($\approx 634 \times 634$ arcsec$^2$) frames cen-
tred on the BCG, using the standard IRAF task GEOTRAN. Pixels are
resampled using linear interpolation and all images are rescaled to
the same metric length at the redshift of the cluster. Considering
the redshift distribution of the sample, we rescale the images such
that 1 Mpc = 629.3 pixel, thus minimizing the average rescaling. In
addition we either apply a random rotation before stacking, or we
align the images based on the BCG orientation. The first method
is more appropriate to study the radial surface brightness profiles,
since it ensures the perfect central symmetry of the stacked images.
Aligning the images to the BCG is most suitable in order to study
the correlation between the two-dimensional shapes of different lu-
minous components, as will be shown in Section 5.3.

Pixel counts are then rescaled in order to remove the effects of
the variation of Galactic extinction and cosmological surface bright-
ness dimming $(1 + z)^4$ between different clusters, and to homoge-
nize the photometric calibration (Fukugita et al. 1996; Hogg et al.
2001; Smith et al. 2002). This was done according to the following
equation:

$$c' = c \times \frac{f_{20,\mathrm{ref}}}{f_{20}} \times 10^{0.4 \times A_\lambda} \times \left( \frac{1+z}{1+z_{\mathrm{ref}}} \right)^4 \tag{1}$$

where $c'$ and $c$ are the counts in a pixel after and before intensity
rescaling, respectively; $f_{20,\mathrm{ref}}$ and $f_{20}$ are the counts correspond-
ing to 20 mag in the arbitrary reference calibration system and in
the frame calibration system respectively; $A_\lambda$ is the Galactic ex-
tinction as reported in the SDSS data base, according to Schlegel,
Finkbeiner & Davis (1998); and $z$ and $z_{\mathrm{ref}}$ are the redshift of the clus-
ter and the reference redshift, that has been chosen to be close to the
median redshift of the sample, that is 0.25. This calculation ignores
*K*-corrections as they are unknown for the ICL and given the small
redshift range probably have negligible effects on our results. In the
following we will always use the subscript '0.25' to refer to magni-

[4] We use SEXTRACTOR version 2.3 throughout the present work.

tudes and surface brightness in the photometric system defined by
equation (1).

Masks 'A' and 'B' are built for each cluster from an analysis of
the original corrected frames, and then geometrically transformed
to match the corresponding images. First we build the 'B' mask for
the saturated sources and the stars in the field. Relying on the SDSS
photometric data base, we select all objects which are flagged as
saturated and lie within 10 arcmin of the BCG. These are masked
out to an extent of three times the maximum isophotal radius in the
three bands, in order to avoid including scattered light or their bright
extended haloes in the stack. All stars brighter than 20 mag in *r*-band,
with isophotal radius measured in at least two bands, are identified
and masked out to their maximum isophotal radius in the three
bands. The magnitude limit is chosen such that less than 1 per cent
of objects classified as stars by the photometric pipeline are likely to
be misclassified galaxies (see Ivezić et al. 2002). This allows us to
minimize the foreground signal, while losing a negligible fraction
of light from cluster galaxies. However, a small fraction (less than
10 per cent) of bright non-saturated stars are left unmasked because
they do not have good isophotal measurements. Since these stars
are randomly located in the frames, no systematic effects on our
measurements are expected, although this failure increases the noise
in the foreground signal.

To obtain the 'A' mask we run SEXTRACTOR on the frames in
the three bands, using a Gaussian smoothing kernel (FWHM =
4.0 pixel), a minimum detection area of 10 pixel and detection
thresholds corresponding to $\mu_{r,0.25} = 24.5$, $\mu_{g,0.25} = 25.0$ and
$\mu_{i,0.25} = 24.0$ mag arcsec$^{-2}$. We blank the segment correspond-
ing to the BCG in the segmentation images and OR-combine them
with the 'B' mask previously generated to get the final 'A' mask.
Note that both the 'A' and the 'B' masks are the same for all the
three bands, thus allowing a consistent measurement of the colours.

The stacking of the images is performed using the standard IRAF
task IMCOMBINE. The images in each (sub)sample are combined with
a simple average of the pixel counts, excluding the masked pixels.
We do not apply any kind of statistical rejection to the pixel count
distributions, since we cannot assume that the light follows the same
distribution in all clusters on a few-pixel scale. This is obviously not
the case when considering the total light which is dominated by the
galaxies, but even for the diffuse component significant substructure
can be present as well (see e.g. Gregg & West 1998; Trentham &
Mobasher 1998; Calcáneo-Roldán et al. 2000).

## 4 THE PHOTOMETRIC ANALYSIS

In Fig. 4 we present the central $\sim$600 kpc of the stacked images in
the total sample, for the diffuse component plus BCG ('A' masks,
left panel) and for the total emission ('B' masks, right panel). In
order to increase the S/N, the *r*- and *i*-bands have been combined in
these plates using a weighted average of the intensities, where the
weights are given by the inverse square of the rms of the intensity
in each stacked pixel. The combined intensities are translated into
AB mag for a combined $r + i$ passband, whose effective response
function is given by the sum of the two filter responses. Scales are
marked in kpc. In panel (a) we superpose the isophotal contours
corresponding to 26, 27, 28, 29 and 30 mag arcsec$^{-2}$ in the $r +
i_{0.25}$-band, obtained smoothing the original image with kernels of
increasing size, as described in the caption. Corresponding surface
brightness (SB) values in *r*-band are $\sim$0.3 mag brighter.

In both panels the central region ($R \lesssim 100$ kpc) is dominated
by the BCG, which has not been covered by either the 'A' or 'B'
masks. Given the circular symmetry of the stacked images and the
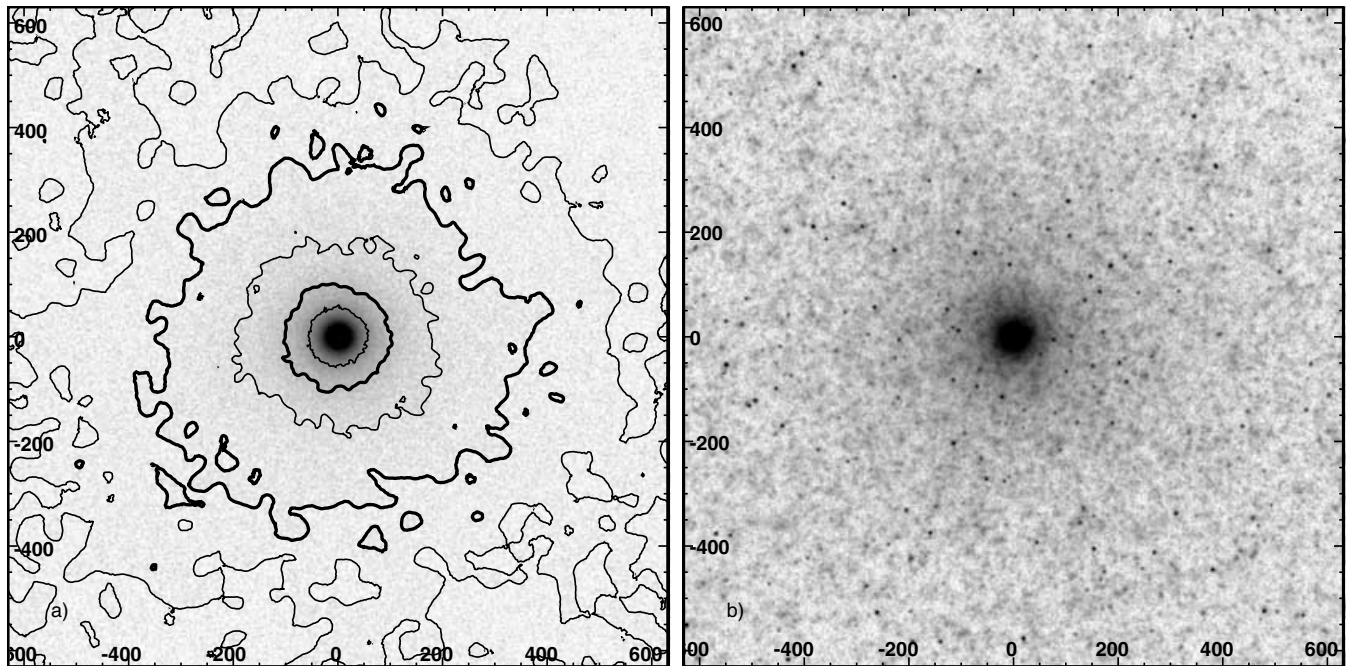
**Figure 4.** The $r + i$ composite images resulting from the stacking of the main sample: the diffuse component plus BCG is in panel (a), the total light in panel (b). The same logarithmic grey scale is adopted in both images. Side-scale tick-marks display the distance in kpc from the centre. Isophotal contours corresponding to $\mu_{(r+i),0.25}$ of 26, 27, 28, 29 and 30 mag arcsec$^{-2}$ for the diffuse component are overplotted on panel (a). Smoothing kernels of 3, 7, 11, 17, and 21 pixel, respectively, are used. Corresponding SB values in $r$-band are ~0.3 mag brighter. Note the point-like sources in panel (b), which are the stars left unmasked due to the failure in the measurements of their isophotal radii, as mentioned in Section 3.

need to integrate over large areas to increase the S/N, we perform the photometric analysis in circular apertures. The stacked image is first divided into a number of circular annuli, centred on the BCG and logarithmically spaced. Within each annulus, the average surface brightness is computed simply by summing the intensity in the pixels and dividing by the total number of pixels. The logarithmic spacing ensures that a larger area is summed at large radii, where the signal is lower. In order to evaluate the statistical uncertainty on the computed SB, we further divide each annulus into a number of sectors with aperture angle $\theta \simeq \Delta R/R$, where $\Delta R$ is the thickness of the annulus and $R$ its average distance from the centre. The rms of the SB among the sectors is thus representative of the SB fluctuations on the typical spatial scale covered by the annulus; the statistical error on the average SB is then just given by the rms divided by $\sqrt{N-1}$, $N$ being the number of sectors in the annulus.

Background estimation is a critical issue when attempting to measure very low surface brightnesses, which are just a few $\sigma$ above the noise. In particular, when integrated fluxes over large areas are estimated, the uncertainty on the background level dominates the measurement error.

Due to the limited spatial coverage provided by the individual SDSS frames, at $R \gtrsim 1$ Mpc and beyond, the fraction of stacked images which contribute to the intensity of each pixel drops below 50 per cent. Given the average $R_{200}$ of 1.1 Mpc for the clusters in the main sample,[5] we cannot directly estimate the background level around the stacked cluster images. Since the mean galaxy profile of clusters is known to follow the analytical profile proposed by Navarro, Frenk & White (1995) (NFW, see, for example, Carlberg

et al. 1997), we estimate the background SB level in the stacked images by fitting a projected NFW profile (see Bartelmann 1996) plus a constant to the SB profiles extracted before. The fitting is performed between 100 and 900 kpc, the innermost 100 kpc being excluded because of the predominance of the de Vaucouleurs profile (de Vaucouleurs 1948) of the BCG in these central regions. The best-fitting value of the constant is used as the residual background level, which may be positive or negative, since a sky background has already been subtracted from each individual cluster image based on the mean sky surface brightness 1 Mpc away from the BCG. The corresponding uncertainty is given by the square root of its variance as determined from a set of Monte Carlo realizations of the measured profile, where the intensity in each point is randomly varied according to the associated error. In Section 7 we will discuss in further detail the validity of this method.

### 4.1 Definition of the ICL and corrections for mask incompleteness

A measurement of the intracluster light, conventionally defined as the luminous emission from stars which are unbound to any individual galaxy, would require a fully dynamical characterization of such stars. This is completely beyond our observational capabilities. Based on purely photometric properties, the most sensible and robust definition of the ICL is the emission coming from outside the optical boundaries of individual galaxies. Given the properties of our data set, we define the optical boundary as the $\mu_{r,0.25} = 25.0$ mag arcsec$^{-2}$ isophotal contour. This does not encompass the low surface brightness emission from the outermost parts of galaxies, so a fraction of what we define as ICL will actually come from stars bound to galaxies, as we will argue more quantitatively in Section 5.4.

---

[5] This is consistent with a mean mass of $7-8 \times 10^{13}$ M$_\odot$.

In addition to this contribution which is inherent to our definition of the ICL, contamination arises also from incomplete masking (i.e. from masks failing to cover the entire optical extent of a galaxy) and from undetected galaxies. We have tested the efficiency of our masking algorithm on a mock data set of ∼650 simulated clusters. In order to reproduce the observational properties of the real sample, we use the same redshift, Galactic extinction, background noise properties, point spread function (PSF) and photometric calibration parameters as in the real cluster sample.

For each simulated cluster, we generate 1000 random galaxies whose photometric properties are assigned as follows. First we draw their absolute *r*-band luminosity from a Schechter luminosity function (LF), using the fitting parameters of Mobasher et al. (2003) ($\alpha = -1.18$, $M^*_R = -21.79 + 5 \log h_{65}$),[6] who studied the LF of the Coma cluster down to $M_R = -16 + 5 \log h_{65}$. Using the data in Blanton et al. (2003b), we have computed the two-dimensional conditional probability function $P(n, \mu_e | L)$ of the Sérsic index $n$ and $\mu_e$ for a given luminosity $L$. According to this, we assign random $n$ and $\mu_e$ to each galaxy. A projected axial ratio is randomly drawn from a Gaussian distribution centred at 0.7 and with $\sigma = 0.25$ (we assume that clusters are dominated by early-type galaxies and use the results in Lambas, Maddox & Loveday 1992), the orientation is random.

The model SB distribution in the $r_{0.25}$-band is then computed *out to the optical radius* (as defined above). Size and intensity are rescaled according to the redshift,[7] Galactic extinction and photometric calibration of the corresponding observed cluster. The model distribution is sampled on the pixel array. The resulting image array is then convolved with the PSF and the sky background is added. Finally we add Poisson noise, using the actual electron-to-ADU conversion factor of each frame. We use the average colours of the total light in the stacked images to derive from the $r_{0.25}$-band model image the corresponding mock frames in the *g*- and *i*-bands.

The mock images are processed with the same codes and algorithms used for the real ones, and stacked. We find that roughly 15 per cent of the light in the *r*-band within the optical radius of the simulated galaxies fails to be blocked by our masking algorithm, because of partial or complete non-detections. Very similar amounts are missed in *g* and *i*. These results clearly are expected to depend on the shape of the luminosity function of the cluster galaxies, and particularly on the slope at the faint-end. In fact a steeper faint-end and/or a fainter $M^*$ can produce significantly higher contaminating fractions, and vice versa. We will discuss the systematic uncertainty deriving from the choice of the LF in further detail in Section 6.2. Throughout the rest of the paper we will adopt the corrections based on the Mobasher et al. (2003) LF as our fiducial corrections.

Assuming that the fraction $f$ of unblocked galaxy luminosity is roughly independent of clustercentric distance, we can compute the corrected surface brightness of the ICL:

$$\Sigma_{\text{ICL}} = \frac{1}{1-f} \times \Sigma_{\text{diffuse}} - \frac{f}{1-f} \times \Sigma_{\text{total}} \qquad (2)$$

[6] This corresponds to $M^*_r = -21.37 + 5 \log h_{70}$ using the photometric conversion provided by the Bruzual & Charlot (2003) code for a 13-Gyr old, solar metallicity simple stellar population (SSP).

[7] We adopt a uniform *K*-correction within each cluster, namely the one for a spectral energy distribution of a simple stellar population formed 10 Gyr ago with solar metal enrichment (Bruzual & Charlot 2003).

where $\Sigma_{\text{diffuse}}$ and $\Sigma_{\text{total}}$ are the surface brightness as derived from the stacked images masked with the 'A' and 'B' masks, respectively.

## 5 RESULTS

### 5.1 Surface brightness profiles

We present the results of our photometric analysis for the main sample in Fig. 5. In the first three panels (a)–(c) we show surface brightness profiles for various cluster components (lower plots) as well as the local ratio of ICL+BCG to the total cluster light (upper plots) for the *g*-, *r*- and *i*-bands. The radial coordinate is scaled to $R^{1/4}$. In the SB profile plots, triangles with error bars (red online) represent the average *total* SB, including all cluster components, whereas black open circles are the SB of the *diffuse* component (ICL+BCG). The SB of the ICL+BCG component after correcting for the contamination due to mask incompleteness is shown by black filled circles with error bars. For the *total* SB, error bars represent the maximum range of variation when allowing for 1σ uncertainties in the background level and in the local estimate of the SB. For the ICL+BCG component the analogous maximum range of variation is computed taking errors on both *total* and *diffuse* light measurements into account, after combining them with the standard error propagation formulae applied to equation (2). The two horizontal lines display the SB corresponding to 1σ background uncertainty, for the *total* light (dashed line, red online), and for the *diffuse* light (solid line).

The profiles can be reliably traced out to ∼700 kpc at the level of $\mu_{r,0.25} \sim 32$ for the ICL ($\mu_{r,0.25} \sim 31$ for the uncorrected *diffuse* component) and $\mu_{r,0.25} \sim 29$ mag arcsec$^{-2}$ for total light (5σ detections are obtained at 500 kpc in all bands).

As is apparent from the straight-line behaviour in all three bands, in the inner 40–50 kpc the SB profile of the ICL+BCG component closely follows a de Vaucouleurs law. We fit this law to the inner points of the profiles using an iterative procedure based on standard least squares. We start fitting between 10 and 20 kpc to ensure that we exclude the innermost region, where the seeing (FWHM ∼ 5 kpc at the average redshift of the clusters) is likely to affect the measured profile significantly. Outer points are added iteratively until the error on the slope is increased by more than 10 per cent with respect to the previous step. The last two points are then discarded and the fitting parameters are recomputed.

The best-fitting de Vaucouleurs law to the inner ICL+BCG profile is plotted as a dotted line in the lower section of panels (a)–(c) of Fig. 5. The effective radius $R_e$ is marked with a vertical dashed line and fitting parameters are reported nearby. Typical errors are ∼10 per cent on $R_e$ and ∼0.1 mag arcsec$^{-2}$ on $\mu_e$. We note that, while the effective radii are consistent in *r* and *i*, in the *g*-band $R_e$ is significantly larger by some 5 per cent. This is consistent with a significant colour gradient in the expected sense within the BCG itself.

Beyond 50 kpc the profiles clearly flatten, both in the ICL component and in the *total* light. Still, there is evidence for the ICL component being more centrally concentrated. The $R^{1/4}$ slope of the ICL component stays roughly constant between 150 and 500–600 kpc, with an equivalent $R_e$ of 250–300 kpc in all three bands. The *total-diffuse* light is also quite well fitted by an $R^{1/4}$ law, but here the equivalent $R_e$ is ∼2 Mpc in all three bands.

The higher concentration of the ICL component with respect to the *total* light is confirmed by the upper sections of the plots in Fig. 5, where we plot the local ratio of the ICL+BCG to the *total* light using black filled circles with error bars. Error bars are computed by combining the errors on the fluxes derived as described above.
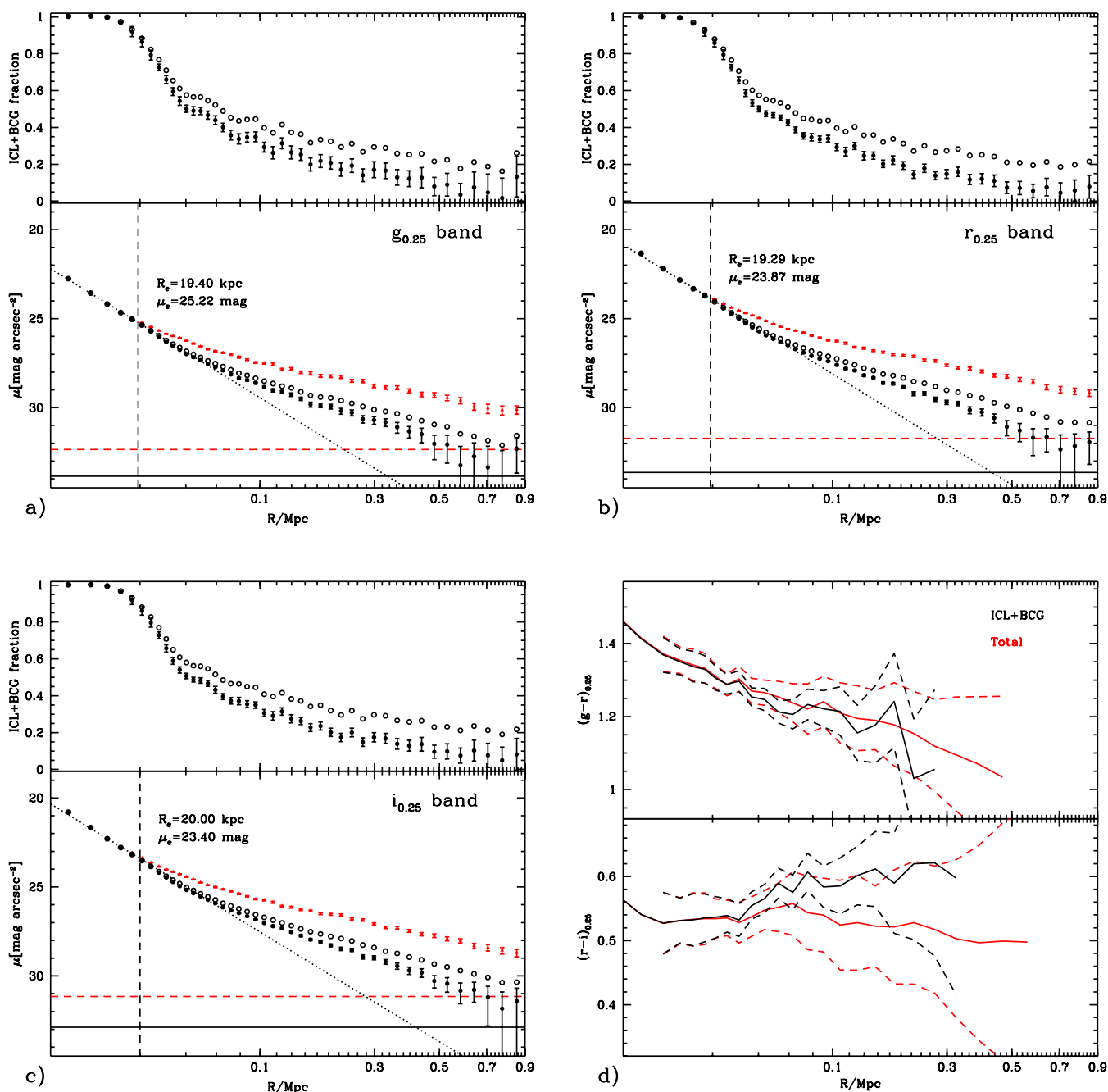
**Figure 5.** Surface photometry of the main sample. Panels (a)–(c) show the surface brightness profiles and the local ratio of ICL+BCG and uncorrected *diffuse* light to the *total* cluster light in the *g*-, *r*- and *i*-bands, respectively; in panel (d) the *g* − *r* and *r* − *i* colour profiles are plotted. The *R*-axis is linear in $R^{1/4}$. Panels (a)–(c), lower section: the SB is expressed in mag arcsec$^{-2}$ in the $z = 0.25$ observer frame. Triangles with error bars (red online) represent the total cluster light, open circles the diffuse light (including the BCG) as directly measured from the stacked images. Filled circles with error bars display the SB of the ICL+BCG, corrected for masking incompleteness adopting the LF given by Mobasher et al. (2003). Horizontal dashed (red) and solid lines display the SB corresponding to the 1σ uncertainties on the background determination for the total light and for the ICL+BCG, respectively. The dotted lines represent the best de Vaucouleurs fits to the inner regions (see text for details): the effective radii of the best-fitting models are indicated with vertical dashed lines and the corresponding parameters are reported nearby. Panels (a)–(c), upper section: the local ratio of ICL+BCG (filled dots with error bars) and uncorrected *diffuse* light (open circles) to *total* cluster light. Panel (d): *g* − *r* (upper section) and *r* − *i* (lower section) colour profiles. Thin lines (red) are used for the *total* light, thick lines for the ICL+BCG component, corrected according to the Mobasher et al. (2003) LF. Dashed lines represent the 1σ confidence intervals.

Empty circles represent the fraction of uncorrected *diffuse* light, that is the upper limit to the ICL fraction when one allows for different choices of the LF.

Excluding the central ∼50 kpc, where the BCG dominates, a smooth monotonic decrease of the ICL fraction is observed all the way out to the limit of significant detections, from ∼50 per cent at 50 kpc down to ≲5 per cent at 600–700 kpc for our preferred faint galaxy correction. By comparing the two fractions, we see that the ICL is the main component of the *diffuse* light out to ∼300 kpc. Outside this radius we must expect that the *diffuse* emission reflects

more and more the properties of faint cluster galaxies rather than those of the ICL.

## 5.2 Colours of the ICL

In panel 5(d) we show the $g - r$ and $r - i$ colour profiles for the ICL+BGC (thick solid lines) and for the total light (thin solid lines, red online). Dashed lines show the $1\sigma$ confidence interval derived from the errors on the fluxes in the different bands. Only data points for which the confidence interval is smaller than 0.5 mag are connected, in order to avoid confusion arising from noisy measurements. We observe a striking consistency between the colours of the *total* emission and those of the ICL+BCG in both $g - r$ and $r - i$ out to 300 kpc, where the light from bound stars in galaxies dominates the *total* emission. There is marginal evidence for slightly redder $r - i$ (+0.03 mag) in the ICL at $R > 100$ kpc, but its significance is low, less than $1\sigma$.

In agreement with the above determinations of $R_e$, within 80–100 kpc we find a clear gradient in $g - r$, from 1.4–1.5 in the centre to ~1.20 at 80 kpc, whereas the $r - i$ profile is consistent with being flat over this radius range, within the errors, with an average value ~0.60. Outside 80 kpc the $g - r$ profile flattens too, both for ICL+BCG and for the *total* light.

## 5.3 Isophotal ellipticity

We now investigate possible relationships between the shape of the BCG and those of the ICL and of the cluster galaxy distributions. We study the isophotal shapes of the ICL and of the galaxy light for two subsamples of clusters in which the BCGs exhibit a clear elongation. The stacking in this case has been performed after aligning the images along the major axis of the BCG. The selection is from the main sample clusters after requiring $m_{r,0.25}(BCG) < 17.90$ to ensure a more reliable estimate of the parameters of the best-fitting two-dimensional de Vaucouleurs model, as provided by the SDSS PHOTO pipeline (Lupton et al. 2001). We choose an axial ratio limit of $b/a_{BCG} < 0.85$, for the first subsample, and a more restrictive limit of $b/a_{BCG} < 0.70$, for the second one. The images are aligned according to the position angle provided by PHOTO. A few clusters, for which the fitting algorithm clearly failed to provide a sensible description of the shape of the BCG, have been rejected after visual inspection. The two final samples contain 355 and 112 clusters.

The analysis of the resulting *diffuse* light image is performed by fitting elliptical isophotes. Such isophote fitting cannot be used for the galaxy light, because of the shot noise arising from galaxy discreteness. We therefore characterize the shape of the galaxy distribution by means of moments of the *total − diffuse* light image. We use $(r + i)$-band composite images derived from the weighted average of the two single bands (cf. Fig. 4), to enhance the S/N.

In the central 50 kpc of the *diffuse* light image the fitting is done using the standard IRAF task ELLIPSE. Outside this radius the S/N is too small to make the fitting method implemented in ELLIPSE applicable. In fact, this method (see Jedrzejewski 1987) consists in minimizing the variance of the intensity along 1-pixel wide elliptical paths by varying the geometrical parameters of the ellipse. In our fitting code the elliptical paths are replaced with elliptical annuli, which are several pixel wide, and the intensity variance is computed not on a single-pixel basis, but using approximately square (side~annulus width), non-overlapping contiguous regions along the annulus. For each given semimajor axis $a$ the width of the elliptical annulus $\Delta a$ is fixed as $a \times 0.2$. The ellipse is aligned with the BCG. We compute
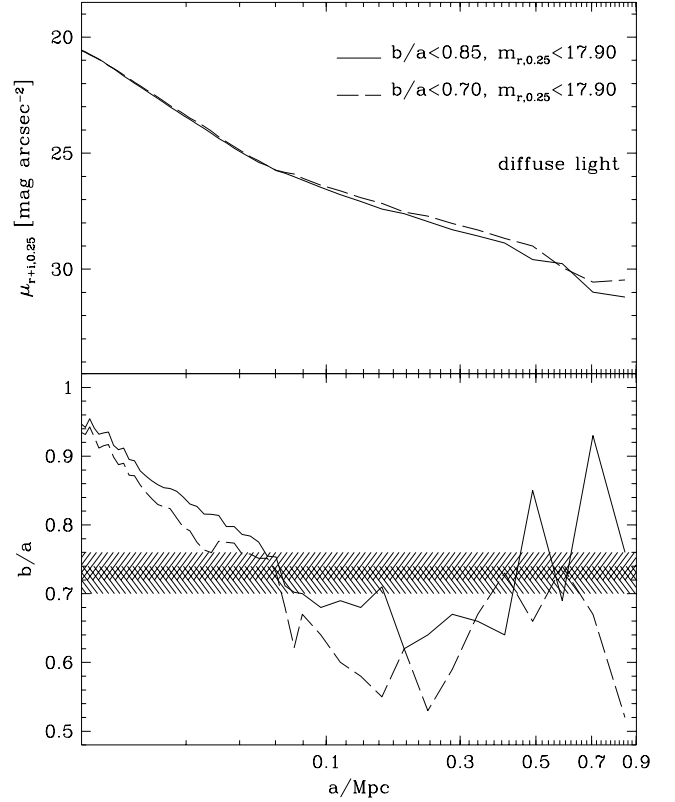


**Figure 6.** Elliptical isophote analysis of the diffuse light of two subsamples of clusters, whose images have been aligned along the position angle of the best-fitting de Vaucouleurs model for the BCG. Only clusters with luminous BCG [$m_{r,0.25}(BCG) < 17.90$] have been stacked. As a function of the semimajor axis $a$ we show the isophotal SB in the $r + i$ composite band (upper panel) and the axial ratio $b/a$ (lower panel). Solid lines are used for the sample with $b/a_{BCG} < 0.85$, dashed lines for $b/a_{BCG} < 0.70$. The shaded regions indicate the mean ellipticity value (plus uncertainty) of the galaxy distribution, with the two different slants representing the two subsamples.

the axial ratio $b/a$ that minimizes the intensity variance using the standard golden section search algorithm, as implemented in Press et al. (1992).

The results of this analysis are shown in Fig. 6, where the two panels display the average SB of the isophotes (upper panel) and the axial ratio $b/a$ of the isophotal ellipses (lower panel). Solid lines are for the sample with $b/a_{BCG} < 0.85$, while dashed lines are for $b/a_{BCG} < 0.70$. Typical errors for $b/a$ range from 0.05 to $\gtrsim 0.10$ going from the centre to 700 kpc. The two samples display very similar behaviour, except for a lower $b/a$ in the sample with flatter BCGs, as expected. We note a progressive flattening of the isophotes from the centre out to $a \sim 150$ kpc. While the smearing effect of the PSF (FWHM $\sim 5$ kpc) is certainly biasing the measurements in the central 10–20 kpc, at larger distances this flattening must be considered real. At $a \gtrsim 500$ kpc, large $b/a$ uncertainties ($\gtrsim 0.1$) do not allow us to establish whether the apparent increasing trend is real or not. As noted above, however, the *diffuse* light is expected to be dominated by unmasked galaxy light at these distances, and therefore does not provide reliable information on the distribution of the ICL.

The flattening of the cluster galaxy distribution is derived from first-order moments of the (*total − diffuse*) light image, $S_x = \sum_i |x_i| F_i$ and $S_y = \sum_i |y_i| F_i$, where the $x$ and $y$ coordinates are aligned with and perpendicular to the BCG orientation, respectively,

$F_i$ is the fraction of light in pixel $i$, and the sums are within an ellipse having 700-kpc semimajor axis and axial ratio $b/a$. The $b/a$ that best fits the flattening of the galaxy light distribution is obtained by requiring $S_y/\ S_x = b/a$. For our two subsamples we obtain $b/a = 0.74 \pm 0.02$ and $b/a = 0.72 \pm 0.02$. These results do not change appreciably for variations of the semimajor axis $a$ in the range 700–350 kpc. The galaxy distribution is thus significantly rounder than that of the ICL between 100 and 400 kpc. In fact, by using the *diffuse* light as proxy for the ICL, we are probably underestimating the real effect. Unless the faint galaxy population that contaminates the *diffuse* light has significantly higher degree of alignment with the BCG than the bright one, the ellipticity we measure in the *diffuse* image should be smaller than in the real ICL.

It is interesting to note that the semimajor axis at which the maximum flattening of the isophote is first reached, $a \sim 100$ kpc, lies somewhat outside the radius where the outer shallower SB profile takes over from the inner de Vaucouleurs and the galaxy component starts dominating the total light.

### 5.4 ICL–galaxy connection

We further investigate the connection between the galaxy distribution and the ICL by studying the photometric properties of the ICL in regions at different projected distances from bright galaxies. First we select all the galaxies more luminous than $M_r^* + 2.0$ mag in the SDSS data base; this corresponds to $m_{r,0.25} < 21.23$ assuming the Mobasher et al. (2003) LF. All pixels contributing to the *diffuse* light image (i.e. not masked according to type 'A' masks) are partitioned into four different classes according to their distance $l$ from the nearest bright galaxy, namely $l < 15$ kpc, $15 \leqslant l < 25$, $25 \leqslant l < 40$, and $l > 40$ kpc. We further distinguish between four different ranges in clustercentric distance: from 100 to 200 kpc, from 200 to 400, from 400 to 750 and from 800 to 900 kpc, this last one being roughly representative of the background. Fluxes in each class of $l$ and clustercentric distance are stacked separately. As the best estimate of the background level we adopt in this case the average surface brightness of pixels in the 800–900 kpc annulus with $l > 40$ kpc.

The results of this stacking are reported in Table 1. The clustercentric distance $R$ (in kpc) is given in column (1); column (2) reports the projected distance $l$ to the nearest bright galaxy (in kpc); the average SB of these pixels is given in column (3), while column (4) displays the fraction of ICL in each annulus contributed by pixels in the specific $l$-range. For the first three classes of $l$ we compute the difference between the mean flux actually measured and the flux that would be measured if those pixels had the same SB as the ones at $l > 40$. The ratio of this flux excess to the *total* ICL flux in the annulus of clustercentric distance $R$ is reported in column (5). Finally, the fraction of pixels with projected distance $l$ to the nearest bright galaxy is given in column (6). The fractions in the last three columns are given in per cent.

In Fig. 7 we plot, with solid lines, the SB of the *diffuse* light in the four classes of $l$ as a function of the clustercentric distance. For the three nearest $l$ bins, the dashed lines represent the SB of the excess with respect to the SB at $l > 40$. We note immediately that the SB around luminous galaxies depends very weakly on the clustercentric distance. This is even more evident if one considers the surface brightness excess plotted with dashed lines in Fig. 7. This light can therefore be seen as representing the stars in the unmasked outer regions of individual galaxies.

The SB excess around galaxies is about a quarter of the total diffuse light in the 100–200 kpc annulus. For 200–400 kpc it is almost half of the *diffuse* light. At 400–750 kpc it accounts for more

**Table 1.** ICL–galaxy connection: SB and relative flux and flux excess of the diffuse light at different distances from bright galaxies.

| $R$ | $l$ | $\mu_{r,0.25}$ | $F$ | $F_{\text{excess}}$ | Area |
|---|---|---|---|---|---|
| kpc | kpc | mag arcsec$^{-2}$ | | per cent | |
| (1) | (2) | (3) | (4) | (5) | (6) |
| 100–200 | | | | | |
| | 0–15 | 25.85 | 5.7 | 5.0 | 0.8 |
| | 15–25 | 26.53 | 13.4 | 10.6 | 3.7 |
| | 25–40 | 27.29 | 16.7 | 9.8 | 9.3 |
| | >40 | 28.24 | 64.2 | – | 86.2 |
| 200–400 | | | | | |
| | 0–15 | 25.96 | 10.0 | 9.7 | 0.6 |
| | 15–25 | 26.77 | 20.2 | 18.8 | 2.6 |
| | 25–40 | 27.76 | 20.6 | 17.0 | 6.6 |
| | >40 | 29.65 | 49.2 | – | 90.2 |
| 400–750 | | | | | |
| | 0–15 | 26.07 | 19.4 | 19.3 | 0.5 |
| | 15–25 | 26.97 | 33.4 | 33.1 | 1.9 |
| | 25–40 | 28.13 | 29.5 | 28.6 | 4.9 |
| | >40 | 31.89 | 17.7 | – | 92.7 |
| 800–900 | | | | | |
| | 0–15 | 26.08 | – | – | – |
| | 15–25 | 27.01 | – | – | – |
| | 25–40 | 28.13 | – | – | – |
| | >40 | – | – | – | – |
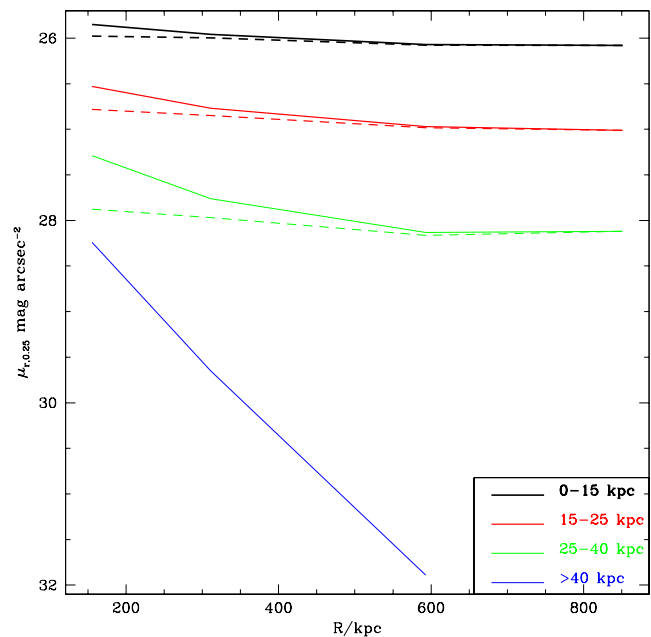


**Figure 7.** SB profiles of regions at different distances from bright galaxies. Line weights (different colours online) correspond to four distance bins, as indicated in the legend. Dashed lines represent the SB excess with respect to regions at distance $l > 40$ kpc.

than three-quarters of the ICL. However, a comparison with the total flux including galaxies shows that the excess flux within 25 kpc represents a fraction between 2 and 7 per cent of the galaxy emission, and thus is well accounted for by the corrections for masking incompleteness described in Section 4.1. The contribution from SB excesses in pixels with $25 < l < 40$ kpc cannot be accounted for by masking incompleteness, both because it is inconsistent with the

estimated corrections and because of the relatively large distance from the galaxies. We therefore conclude that our measurements are consistent with the ICL being dominated by a diffuse emission concentrated in the inner ~300–400 kpc plus a fraction of light clustered around bright galaxies, which dominates in the outer parts.

### 5.5 Dependence on cluster properties: SB profiles

In this section and in the following one we analyse the dependence of the distribution and integrated amount of the ICL on global cluster properties. The description of the subsamples is given in Section 2.1. In order to compensate for the decrease of S/N due to the smaller number of clusters stacked in each subsample, we utilize the $r + i$ composite images, obtained as the weighted average of the final stacked images in the two bands; the weights are given for each

pixel by the inverse variance of the intensity of the corresponding pixels in the images to be stacked.

In the two graphs of Fig. 8 we compare the SB profiles and the ICL fractions of two pairs of subsamples with those of the main sample. In the bottom panels we plot the SB of the *total* light. The panels in the middle display the corrected SB of the ICL+BCG component; the dashed lines represent de Vaucouleurs fits to the inner profiles, derived as explained in the previous section. In the top panels we show the local ratio of ICL+BCG to the *total* light (solid lines) and the same quantity after subtracting the de Vaucouleurs fit to the inner profiles (dashed lines). Intermediate-weight lines (black online) are used for the main sample ('All').

On the left we compare clusters with luminous ('L') and faint ('F') BCGs, using different line weights (red and blue online). The SB profiles are very similar outside 100 kpc, but they are offset, the 'L' clusters being brighter than the main sample, and the 'F'
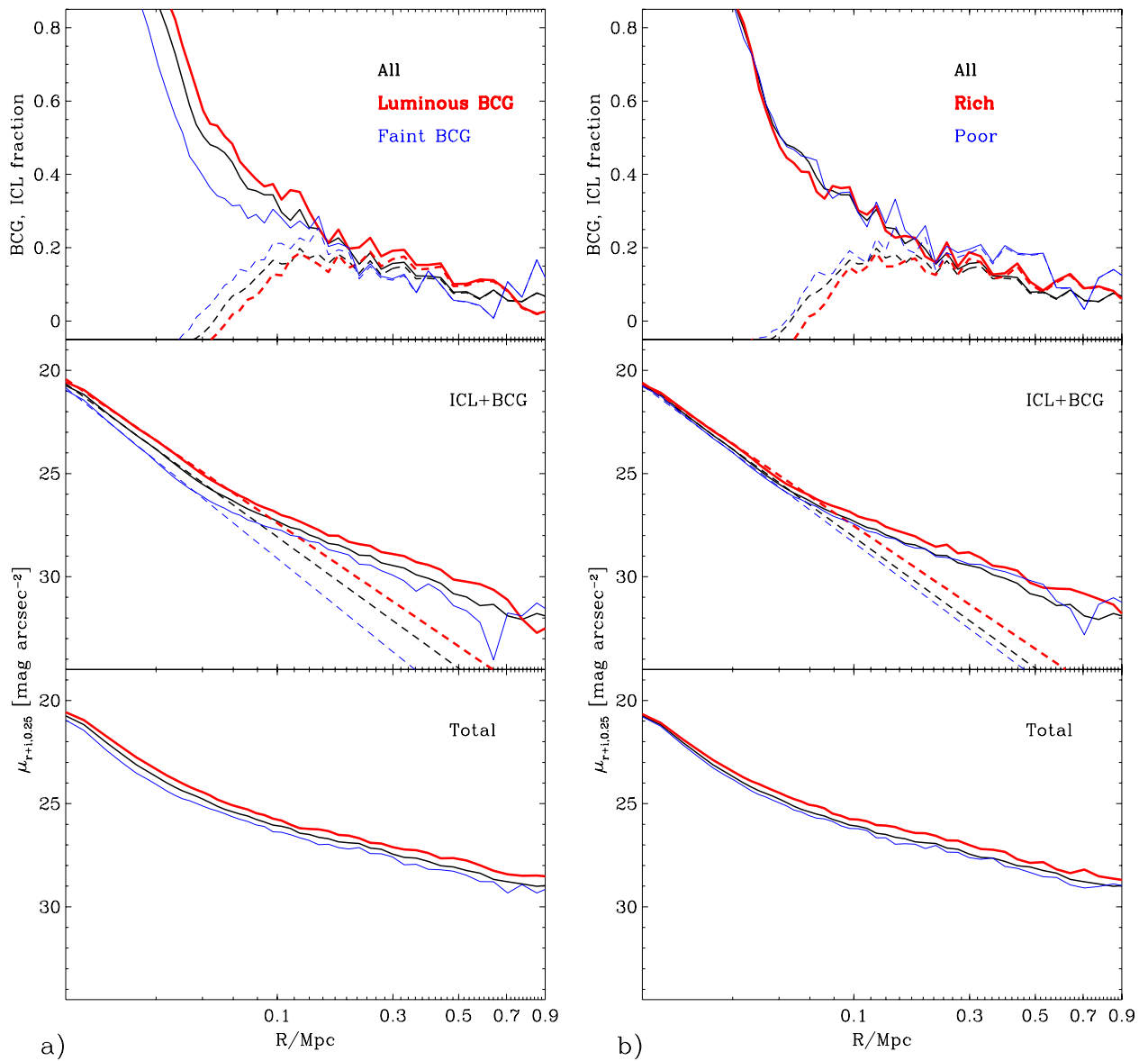


**Figure 8.** Comparison between different subsamples. Intermediate-weight lines (black online) represent the main sample, here shown as reference. Panel (a): clusters with a luminous BCG (thick lines, red) versus clusters with a faint one (thin, blue). Panel (b): rich (thick, red) versus poor (thin, blue) clusters. In the three sections of each panel we plot, from the bottom to the top, the total light SB profile, the ICL+BCG SB profile, with dashed lines representing the de Vaucouleurs fitting to the inner data points, and the ICL+BCG fraction, with dashed lines displaying the ICL fraction after subtracting the inner de Vaucouleurs fitting.

being fainter. Except for the central regions, the offset is similar in the *ICL* and in the *total* light: 'L' and 'F' clusters therefore appear to have a similar relative amount of ICL with respect to the total emission. However, we note a systematic enhancement of the ICL fraction by a few per cent in the 'L' relative to the 'F' clusters. The largest differences are observed in the central regions, where the emission is dominated by the BCG: the most luminous BCGs have larger effective radii ($R_e \sim 23$ kpc) than the mean ($R_e \sim 19$ kpc), whereas faint BCGs have smaller effective radii ($R_e \sim 11$ kpc). The difference in luminosity of the de Vaucouleurs fits to the two classes is a factor of 2.3.

The comparison between clusters of different richness, as determined from the number of red-sequence galaxies, is illustrated by the graphs on the right. Here the thickest lines (red online) represent rich clusters ($N_{gal} > 22$), while the thinnest lines (blue online) are used for poor clusters ($N_{gal} < 17$). Again we observe a great similarity between the profiles. As expected, richer clusters are brighter than the mean, and poor clusters are fainter, both in the *total* emission and in the ICL. Within 700 kpc the ratio of the *total* luminosities of the two classes is 1.8 (1.7 for the ICL). The effective radius of the central $R^{1/4}$ profile is somewhat larger in the rich clusters ($R_e \sim 23$ kpc, similar to 'L' clusters), than in the poor ones ($R_e \sim 16$ kpc, close to the average value, and significantly larger than in 'F' clusters). At $R > 100$ kpc the rich clusters exhibit significantly higher SBs with respect to the mean, whereas the poor ones are only slightly fainter. Considering the large uncertainties in the profile of the poor clusters beyond 400 kpc, the fractions of ICL appear to be fully consistent between the different richness subsamples, ranging from 20 to 5 per cent approximately over the radius range 150–500 kpc.

In Fig. 9 we compare the same four subsamples, by plotting the difference in SB with respect to the mean profile, for the *total* light (bottom panel) and for the ICL+BCG component (top panel). Different samples are represented with different lines as indicated in the legend. In the inner 100 kpc we clearly see that the largest differences are observed between the 'L' and 'F' subsamples. This is not surprising, since this is the region where the BCG dominates. Although the cluster richness correlates with the luminosity of the BCG, clusters in the same richness class can have different BCG luminosity, thus making the separation between rich and poor clusters relatively small in the centre. At larger radii the influence of the BCG is smaller, and the total SB is almost equally affected by the richness parameter and by the BCG luminosity. Nevertheless, the SB of the ICL appears more strongly suppressed in 'F' clusters than in the poor ones.

### 5.6 Dependence on cluster properties: integral photometry

We further investigate the dependence of the relative luminosity of the cluster components on the BCG luminosity and on the richness by analysing the integrated photometry of the stacked $r + i$ images of a set of smaller subsamples. The main sample is thus divided into five subsamples according to $m_{r,0.25}$(BCG), and five subsamples in $L_{RG}$. The $m_{r,0.25}$(BCG) subsamples comprise roughly 140 clusters each, while those in $L_{RG}$ have 170 clusters each in the three lower luminosity classes, and 110 and 60 clusters each in the two bins at the highest luminosities (these different numbers derive from the skewness of the $L_{RG}$ distribution). The total luminosity of the red-sequence galaxies $L_{RG}$ is used here as a proxy to the richness instead of the number of red galaxies, because of its property of being a continuous rather than a discrete variable (see Section 2.1). In each subsample and for each cluster component (galaxies, BCG, ICL) we measure the integrated flux within 500 kpc, and express this
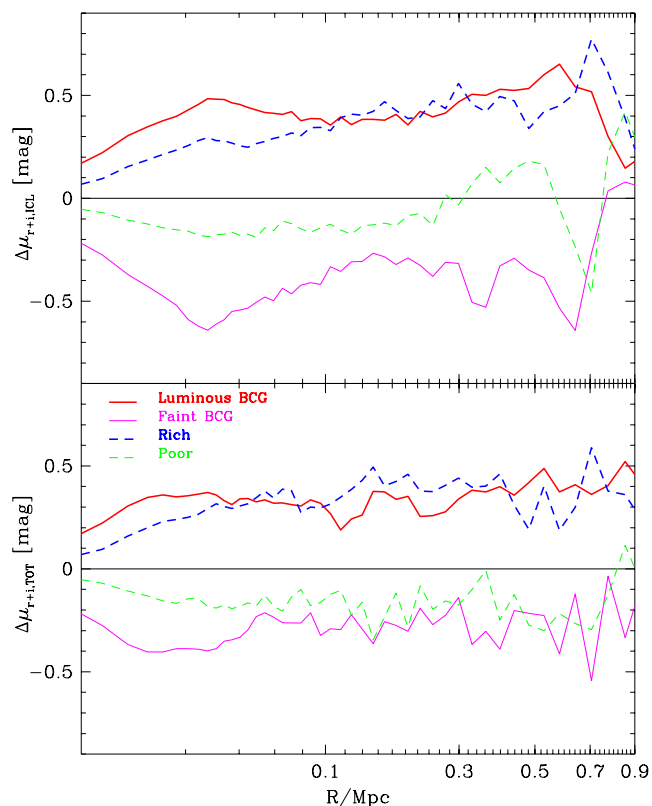


**Figure 9.** Comparisons between different subsamples: SB difference between the subsamples and the main sample. Thick solid lines (red) are used for clusters hosting a luminous BCG, thin solid (magenta) for faint BCG, thick dashed (blue) for rich clusters, and thin dashed (green) for poor clusters. The bottom panel displays the SB differences as a function of the radius for the *total* light, the top panel those for the corrected ICL+BCG component alone.

as a fraction of the total. The total flux is obtained directly from the *total* light images. The corrected ICL+BCG flux is split into a BCG component and the ICL. The BCG flux is given by the integrated flux within the radius out to which the inner de Vaucouleurs profile is fitted plus the integral of the fitting profile extrapolated to the outer boundary, while the remaining corrected ICL+BCG flux is attributed to the 'pure' ICL. Finally, the galaxy flux is just given by the difference between the *total* and the corrected ICL+BCG flux.

The same analysis for the complete main sample yields a ratio galaxies:BCG:ICL of 67.2:21.9:10.9 (uncertainty about ±1.0). Note the small size of the errors here, which is a consequence of our very large sample.

The results for the subsamples are reported in Fig. 10, as a function of $m_{r,0.25}$(BCG) (left panel) and $L_{RG}$ (right panel). The vertical error bars on the fluxes and fractions take into account background uncertainties and surface brightness fluctuations within the apertures; no error on the de Vaucouleurs fit to the BCG is included. We caution that such error bars must be regarded as representing the formal photometric errors in the stacked images, and do not reflect a fully realistic estimate of the total uncertainties. These can be inferred approximately from the scatter of values from our five independent subsamples around any smooth trend. The horizontal error bars cover the range of luminosity included in each subsample, while the point is plotted at the average value.
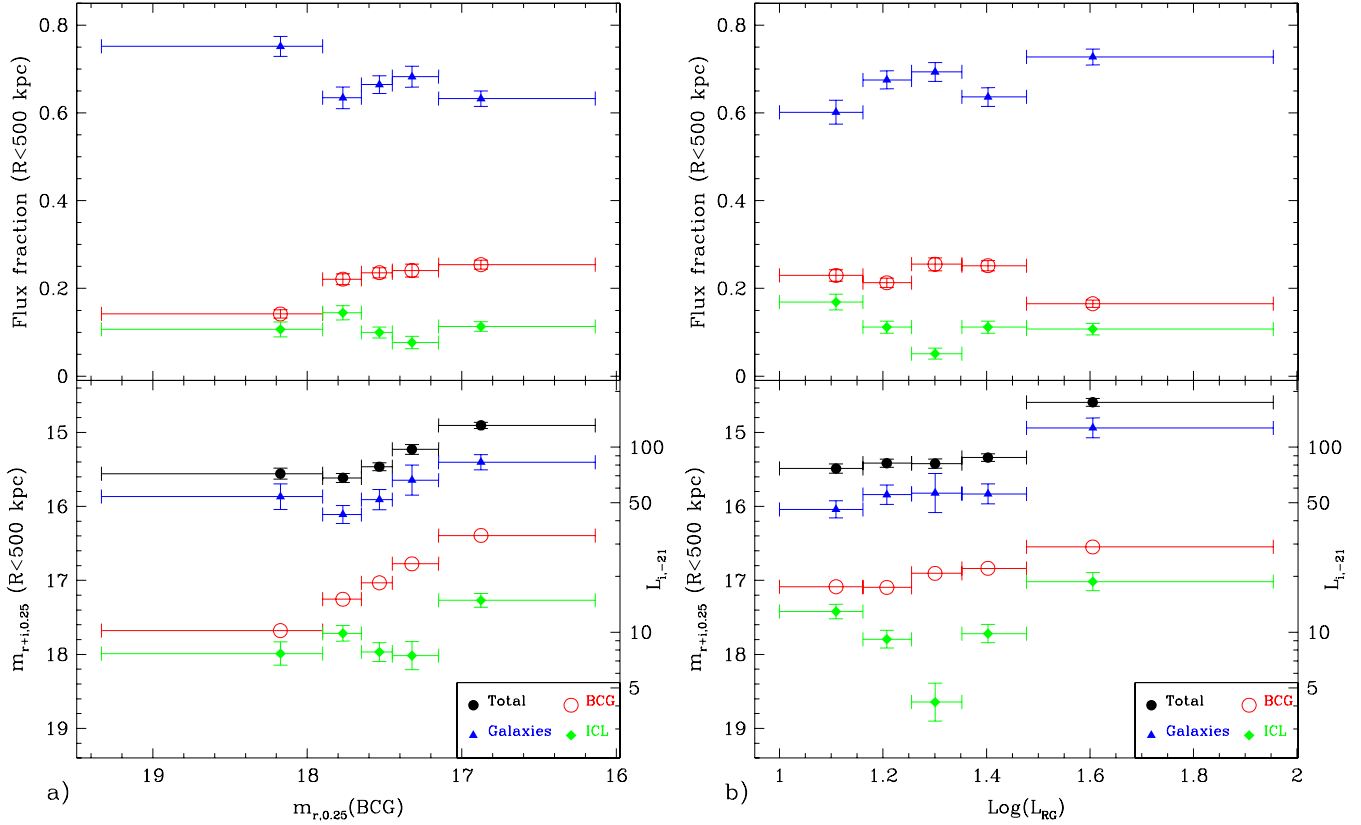
**Figure 10.** The dependence of the integrated magnitude within 500 kpc (lower section) and of the relative fraction (upper section) of different cluster components on the luminosity of the BCG (panel a) and on the total luminosity of the red-sequence galaxies (panel b). BCG luminosity is expressed as $z = 0.25$ observer frame $r$ mag, while the total luminosity of the red-sequence galaxies is given in units of luminosity corresponding to $-21$ absolute $i$-band mag. The integrated luminosities are expressed in $m_{(r+i),0.25}$ and in units of $-21$ absolute $i$-band mag on the left side and right side axis, respectively. Different symbols (and different colours online) are used for the different components as indicated in the legend box. Horizontal error bars show the range of luminosity encompassed in each of the four bins, whereas the vertical error bars display the uncertainty due to the background fluctuations.

Starting with the flux enclosed within 500 kpc as a function of $m_{r,0.25}$(BCG) (Fig. 10, left panel), we note that the luminosity of the galaxy component displays a weak correlation with the luminosity of the BCG, whereas only the clusters with the most luminous BCGs have significantly higher ICL luminosity. The fraction of light provided by the BCG increases from 15 to 25 per cent from the lowest bin to the highest ones, whereas the fraction contributed by galaxies decreases from 75 to 63 per cent. The ICL percentage, instead, is almost constant around 10 per cent.

As a function of the luminosity on the red sequence (Fig. 10, right panel), we observe weak trends in the total luminosity and in the galaxy and BCG emission. Although the brightening of $\sim$1.1 mag in the galaxy component is roughly consistent with the increase of 0.5 dex in $L_{RG}$ over our five bins, a very weak correlation is seen in the four lowest bins. The richest clusters display substantially higher total and galaxy luminosities. Though shallow, a clear correlation between BCG luminosity and richness is present. The richest clusters appear also to have the most ICL. Focusing on the relative fractions, we observe no significant trend in all components in the four lowest bins: the BCG component represents $\sim$23 per cent of the total luminosity, the galaxies $\sim$67 per cent and the ICL $\sim$ 10 per cent. In the richest clusters the contribution of galaxies grows to 73 per cent, that of the BCG decreases to 16 per cent, while the ICL is responsible for $\sim$11 per cent of the total flux, as in the other bins.

In both these plots it is consistent to interpret all variations about the mean ICL fraction of 10.9 per cent just as due to sampling error, which we can estimate at around 3–5 per cent.

## 6 SYSTEMATIC UNCERTAINTIES

The results presented in the previous sections are affected by systematic uncertainties that arise from the methods adopted to estimate the background level and the contamination from galaxy light that fails to be masked. In this section we address these issues by analysing the origins and quantifying the possible amount of such systematic errors.

### 6.1 Background subtraction

As explained above, the background subtraction is based on fitting an NFW profile plus a background constant to our raw SB profiles. From previous studies (e.g. Carlberg et al. 1997) we know that the NFW profile fits well the mean number density profile for galaxies in clusters. Thus our method appears rigorously justified as far as the galaxy light is concerned, provided one excludes the cuspy profile of the BCG. Given that the galaxy component is dominant, especially at large clustercentric distances, the NFW approximation should hold for the *total* light profile too. On the other hand, there is no reason a priori to expect the ICL to follow any particular fitting

**Table 2.** Fraction of unmasked light $F$ from galaxies of different $M_r$.

| $M_r$ | $-22.0$ | $-21.0$ | $-20.0$ | $-19.0$ | $-18.0$ | $-17.0$ |
|---|---|---|---|---|---|---|
| $f$ (per cent) | 2.74 | 5.02 | 8.83 | 18.21 | 67.40 | 99.67 |

function. Nevertheless, we find that the NFW profile is a reasonably good approximation to our ICL profile (with an average chi-squared per degree of freedom of ∼1.5). Since we are interested only in a smooth and physically reasonable extrapolation of the SB profile and given that the extrapolation required is tiny (the last measured points are just 31–31.5 mag arcsec$^{-2}$ above the background), the use of the NFW law appears justified for the ICL as well.

Note that the background uncertainties used in the previous section just take statistical uncertainties in the fitted background level into account. Different choices for the background subtraction strategy can yield results differing by up to a few per cent in the integrated fluxes. Considering the SB profiles, the influence of any reasonable systematic shift of the background level is negligible for all the points within 500 kpc. The use of extended image stripes from continuous SDSS scans would, in principle, provide sufficient coverage to estimate directly the background level at large clustercentric distances ($\gtrsim 2\,R_{200}$). We will test this possibility in future work.

### 6.2 Corrections for mask incompleteness

In Section 4.1 we have computed the fraction of galaxy light that escapes our masking algorithm, based on the observed surface brightness profiles of galaxies of different luminosities, and assuming that the number of galaxies as a function of absolute magnitude is well represented by the luminosity function (LF) of the Coma cluster (Mobasher et al. 2003). This is the best-studied LF in a rich, massive, regular galaxy cluster, and extends to quite a faint limit $M_R = -16$; thus our choice is justified. However, the LF of a single rich, massive, regular cluster at the present epoch may not be representative of the broad range of luminosities covered by our sample at redshift 0.25 (corresponding to ∼20 per cent of the cosmic time). Therefore, it is worth investigating how the fraction of light that is missed by our masks changes if a different LF is used and trying to constrain the possible LF with the available photometric data.

First, using images simulated as described in Section 4.1, we evaluate the fraction of unmasked light as a function of the absolute $r$ magnitude of a galaxy and analyse which galaxies are the main contributors of unmasked light. We estimate its total relative amount in a range of Schechter function parameters and infer the resulting ICL fractions.

The fraction $f$ of unmasked light for galaxies of different absolute $r$ magnitude is reported in Table 2.

Values are close to 0 for bright galaxies. They smoothly increase up to roughly 0.1 for galaxies of $-20$, and then there is a significant upturn at $-19$, which leads to most of the light of faint galaxies being missed by our masks. By integrating over the entire LF[8] we are then able to derive the relative galaxy luminosity that contributes to the diffuse component. In Fig. 11 the unshaded histogram shows the relative contribution of galaxy light in different bins of absolute $r$-band magnitude, according to the Coma LF, while the shaded histogram represents the fraction of unmasked light. The first (last) bin includes also the contribution from all the galaxies brighter (fainter) than the nominal value. While the distribution of galaxy light peaks
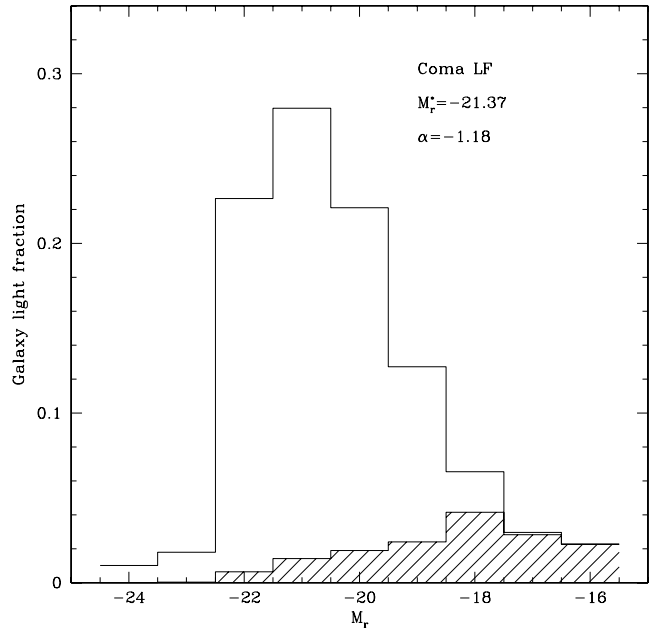


**Figure 11.** The fraction of galaxy light contributed by galaxies of different luminosities (empty histograms), and missed by our masking algorithm (shaded histograms) adopting the Schechter fit to the Coma LF.
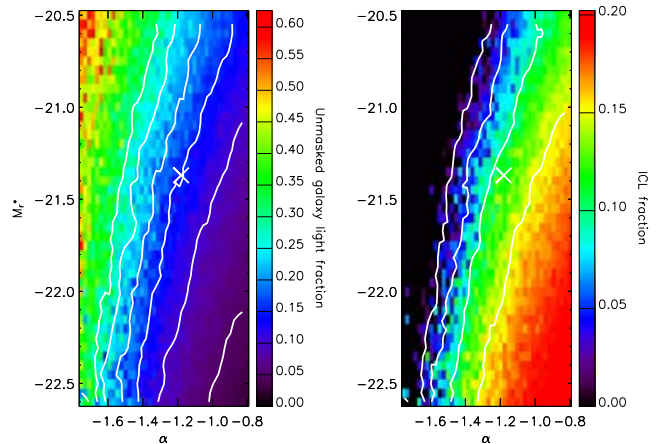


**Figure 12.** Fractions of unmasked galaxy light (left panel) and corresponding ICL estimated fraction (right panels) as a function of the assumed LF parameters, coded in grey-scale levels (colour scale online) according to the legend bars. Contours show curves of equal fractions in 0.05 intervals, from 0.05 to 0.25 for the unmasked fraction, and from 0 to 0.15 for the ICL. The cross represents the location of the Coma LF.

around the characteristic magnitude $M^*$ of the luminosity function, we see that most of the unmasked light comes from galaxies that are at least 2.5 mag fainter than $M^*$.

Dimming $M^*$ increases the contribution of unmasked light from near-$M^*$ galaxies, while steepening the faint-end increases the contribution from faint galaxies. Both variations increase the total fraction of unmasked light. These effects are illustrated and quantified in the left panel of Fig. 12. For a whole range of $(\alpha, M^*)$, the unmasked light fraction is coded by grey-scale levels (colour scale online), as indicated. Lines display the curves of constant unmasked fraction, from 0.05 to 0.25 in steps of 0.05, and the cross corresponds to the Coma LF. Taking this point as a reference, we see that

---

[8] We arbitrarily truncate all the LFs at $M_r > -14.0$, in order to make LFs with $\alpha \leqslant -1$ integrable. Galaxies fainter than this limit contribute less than 0.1 per cent of the total luminosity in the range of parameters explored.

steepening the faint-end by 0.2 can dramatically increase the un-masked fraction to ~25 per cent, whereas dimming $M^*$ by 0.4 mag is required to get to 20 per cent. Going to brighter $M^*$ and less steep slopes, the gradient of unmasked fraction $f(\alpha, M^*)$ becomes shallower, so that a fraction of 10 per cent requires brightening $M^*$ by almost 1 mag, or making the slope shallower by 0.15.

These fractions can be translated into estimates of ICL within 500 kpc, based on the *diffuse* light we have measured, as shown in the right panel of Fig. 12. Similarly to the previous plot, estimated ICL fractions are represented as grey-scale intensities in the $(\alpha, M^*)$ plane. Lines are curves with the same ICL fraction, from 0 to 0.15 in 0.05 steps and the cross corresponds to the Coma LF. The trend is opposite to the previous plot, brighter $M^*$ and less steep slopes implying higher ICL fraction. The range of variation is between 0 and 20 per cent. A very interesting feature of this plot is the presence of a 'zone of avoidance' to the left of the 0 level contour, where the amount of unmasked light would be larger than the *diffuse* light. This excludes all the LFs with very steep faint-end[9] $\alpha \lesssim -1.5$. Applying the same argument to the local fraction of *diffuse* light shown in Fig. 5, we conclude that the fraction of unmasked light cannot be larger than 20 per cent. In turn, this implies (i) that the fraction of ICL integrated within 500 kpc must be at least 6.5 per cent, and (ii) that a faint-end steeper than $\alpha = -1.35$ is inconsistent with our data, unless we assume $M^*$ very different from the reference value for Coma.

As an additional piece of evidence against very steep faint-end LF, we note that the colours of the ICL shown in Fig. 5(d) are the same as or marginally redder than those of the total light. If the ICL was dominated by dwarf galaxies, any reasonable colour–magnitude relation would imply bluer colours than those of the total light.

The natural upper limit to the ICL fraction is given by the fraction of *diffuse* light, that is 21 per cent, which is obtained in the limit of no unmasked light. On the other hand, if we adopt the 'brightest' LF in the literature, namely the one by Goto et al. (2002) ($\alpha = -0.85$, $M_r^* = -22.21$) based on 204 SDSS nearby clusters, we obtain an ICL fraction of 17 per cent ($f = 5$ per cent). This LF has a very bright $M_r^*$ and a very shallow faint-end in comparison to all other measurements in literature.

Although we cannot go very deep and investigate the faint-end, we have measured the composite LF of our clusters (excluding the BCGs) by using the SDSS photometric catalogues and applying statistical subtractions. Our LF is complete to $r = 22$ ($M_r = -18.4$) and clearly indicates that $M^*$ is the same as in Coma within a few 0.01 mag, sufficient to exclude the LF of Goto et al. (2002) as a good description of our clusters and to limit the possible choice of LF parameters.

Adding the fact that, in the light of most of the LF studies in the literature, $\alpha > -1$ seems implausible, we arrive at a tightly constrained region in the space of possible parameters: $M_r^* = -21.37 \pm 0.1$, $-1.35 < \alpha < -1$. This translates into an uncertainty of $\pm 5$ per cent in the estimated fraction of ICL.

## 7 DISCUSSION

In previous sections and particularly in Fig. 5, we have presented surface photometry from the stacking of 683 clusters of galaxies

---

[9] This argument rigorously applies only to a Schechter LF. However, the excess of dwarf ellipticals fainter than $M_R = -15$ found in Virgo (e.g. Trentham & Hodgkin 2002; Sabatini et al. 2003) is unlikely to produce additional contamination larger than 1 per cent.

---

(our main sample). We have been able to measure SB as deep as $\mu_{r,0.25} \sim 32$ mag arcsec$^{-2}$ for the ICL light and $\mu_{r,0.25} \sim 29.0$ for the total light, out to 700 kpc from the BCG. Such SBs translate into rest-frame $g$-band SBs which are roughly 1 mag arcsec$^{-2}$ brighter, as can be easily seen considering the $(1 + z)^4$ cosmological dimming and the fact that the $r$-band at $z = 0.25$ is centred at $\lambda_{\rm eff}' = \lambda_{\rm eff}/(1 + z) \sim 5000$ Å.

Looking at the profiles reported in Fig. 5 we see that: (i) the inner ~50 kpc are well reproduced by an $R^{1/4}$ law; (ii) a significant excess of diffuse light with respect to the inner $R^{1/4}$ law is clearly seen beyond 100 kpc out to 700 kpc; (iii) the SB of the ICL decreases faster than the total SB of the cluster, i.e. the ICL is more centrally concentrated than the light of the cluster as a whole. The inner de Vaucouleurs component is comparable in size with the BCGs observed by Schombert (1986). In fact, the average profile obtained from the stacking of our main sample has an effective radius $R_{\rm e} \simeq 19$ kpc, which roughly corresponds to the median value of $R_{\rm e}$ in his sample.

SB excesses with respect to an $R^{1/4}$ law at large radii ($\gtrsim 100$ kpc) from the BCG have recently been observed by Gonzalez et al. (2005) in a sample of 24 clusters at $0.03 < z < 0.13$. They represent these excesses as a second $R^{1/4}$ component with larger $R_{\rm e}$. Parametrizing the SB excesses in our data in terms of a $R^{1/4}$ law between 150 and 500 kpc, we find an effective radius $R_{\rm e} \sim 250$–300 kpc, consistent with the range of outer $R_{\rm e}$ measured by Gonzalez et al. (2005), although their distribution is peaked at a somewhat lower value, around 100 kpc. However, the ratio of the $R_{\rm e}$ of our two components is 0.06–0.07, fully consistent with their results. The ICL is significantly more concentrated than the total light. Uncertainties or bias deriving from background subtraction and from the estimate of contamination are very unlikely to change this result significantly.

In contrast to our own results and those of Gonzalez et al. (2005), Feldmeier et al. (2004c) have recently claimed that the intracluster star density, as measured from planetary nebulae, does not change as a function of radius or projected galaxy density in the Virgo cluster. This may partly be explained by the young dynamical status of this cluster. However, large field-to-field variations in their estimated SB and their sparse sampling of the cluster region prevent us from drawing firm conclusions. In particular, it is noticeable that the fields at the largest distances from M87 are actually close to M49, which is known to be associated with a major subcluster: it is no surprise, therefore, that the estimated SB in those fields is much higher than expected from any SB–radius relation.

Numerical simulations published to date make a variety of different predictions for the slope of the outer de Vaucouleurs component, ranging from ~400 kpc (Willman et al. 2004) to 70–100 kpc (Sommer-Larsen et al. 2005). Our results seem to favour the models with larger $R_{\rm e}$. It is interesting to note that Murante et al. (2004) produce steeper profiles for the ICL than for the galaxy component in their simulated clusters, and hints of similar behaviour are visible in the simulation of Willman et al. (2004) as well.

Is the measured SB excess contributed by genuine intracluster stars, that is stars orbiting freely in the cluster potential rather than bound to individual galaxies? There are several indications that this is actually the case. The change in slope of the ICL+BCG profile and the change in its colour gradient at $R \sim 70$ kpc suggests strongly that the BCG and ICL components can be considered as distinct stellar populations with different assembly histories. We note that the diffuse light extends continuously well beyond the radius $R \sim 300$ kpc at which the enclosed stellar mass (as traced by the light) begins to be dominated by galaxies other than the BCG. At larger clustercentric distances the dynamics of the diffuse stellar

population must be dominated by the cluster potential, rather than that of the BCG. The fact that we do not see any discontinuity in the diffuse light profile nor any colour gradient going from 100 kpc to the outer regions, lends support to the idea that the stars contributing the SB excess in the inner regions have similar dynamical properties to those at larger distances, and so also orbit freely in the cluster potential.

Based on our analysis of the correlation between the diffuse light and the galaxy distribution, we can exclude the possibility that all or most of the diffuse light is physically linked to individual non-central galaxies, at least at projected radii below 300 kpc. This conclusion is reinforced by the different concentration of the two components.

Surface brightness excesses spatially associated with bright galaxies on scales up to 40 kpc contribute significantly to the ICL. For example, at clustercentric distances of 400–750 kpc, SB excesses surrounding galaxies on this scale sum up to $\gtrsim 80$ per cent of our total measured ICL. From our analysis alone we cannot argue about the origin of this excess. However, observations of individual clusters reported by several authors (e.g. Gregg & West 1998; Trentham & Mobasher 1998; Calcáneo-Roldán et al. 2000; Feldmeier et al. 2002, 2004b), suggest that tidal structures like plumes and arcs may be good candidates for some of it. In fact, smooth bound low-surface brightness haloes around individual galaxies appear unlikely to account for all the light excess, given the large spatial scale, which is larger than the typical optical size of cluster galaxies (e.g. Binggeli, Sandage & Tammann 1985) and comparable with or larger than the expected tidal radii of galaxies in clusters (Merritt 1984).

Further support for our identification of the diffuse light as a distinct component comes from our analysis of isophotal shapes for clusters where the BCG is substantially flattened: in Fig. 6 we have shown that the ICL is significantly more flattened both than the BCG 'core' itself and than the galaxy distribution. Examples of flattening of the outer halo of the BCG with respect to its inner parts have been known since the late 1970s (Dressler 1979; Porter, Schneider & Hoessel 1991), as an association with a similar flattening of the galaxy distribution (e.g. Binggeli 1982). Our ellipticities and the corresponding radial dependences are completely consistent with those of Gonzalez et al. (2005). Moreover, extending the observed radial range well beyond 100–200 kpc, we can present evidence for an asymptotic value for this ellipticity, which is only suggested by their data, although predicted by the two-component de Vaucouleurs models which they fit to the BCG+ICL surface brightness distribution. The fact that this asymptotic ellipticity is first reached where the slope of the SB of the diffuse light flattens lends further support to the hypothesis of a distinct second component responsible for the outer profile. In addition to this, it is intriguing that the change in slope and ellipticity occurs where the galaxy component begins to dominate the total SB, apparently establishing a link between the galaxies and the 'true' ICL.

During the last decade many attempts have been made to assess the total amount of ICL and its contribution to the total cluster light. Current estimates based on different methods range from less than 10 per cent for poor groups of galaxies (Feldmeier et al. 2004a) to $\lesssim 20$ per cent for non-cD clusters (Feldmeier et al. 2004b), to 20–40 per cent for cD clusters (Schombert 1988; Feldmeier et al. 2002) and up to $\sim 50$ per cent for Coma ($R \lesssim 500$ kpc, Bernstein et al. 1995, but at $<25$ per cent according to Melnick et al. 1977). The results presented in Section 5.6 indicate that in the mean the ICL contributes $10.9 \pm 1$ per cent of the flux within 500 kpc, while the de Vaucouleurs component of the BCG contributes $21.9 \pm 1$ per cent. We warn that the uncertainties reflect the measurement errors

only, and we expect the overall uncertainty (sampling plus systematic) in this measure to be about 5 per cent for the ICL and 3 per cent for the BCG. Variations between individual clusters are of course likely to be much larger. Our results thus favour a quite low average ICL fraction, compared to previous estimates. This conclusion is not particularly biased by the properties of our sample, where intermediate and low mass clusters dominate: similar fractions are obtained almost independent of cluster richness and BCG luminosity. This apparent discrepancy points to the problem of how estimates of ICL are derived with different methods and to the need to obtain reliable cross-calibrations.

In our analysis of different subsamples, binned in luminosity of the BCG and in richness, we found that richer clusters, and those with a more luminous BCG, have brighter ICL than poor clusters or clusters with a faint BCG. If we consider the local ICL fractions, however, the variations between different classes are no more than $\pm 5$ per cent, because the total SB varies roughly in the same way as that of the ICL. On the other hand, binning the clusters in finer $L(\text{BCG})$ and richness classes, we found that a significantly higher ICL luminosity within 500 kpc is measured only in the richest clusters and those having the most luminous BCGs, while no trend is observed in the other classes. As already stated, the fraction of ICL instead is roughly constant, within the uncertainties and the sample variance.

We stress that the quoted luminosities are integrated within fixed metric apertures in all our subsamples. These apertures correspond to different fractions of the virial radius in different clusters and this must be taken into account when comparing our results with fluxes and fractions computed within the virial radius. In fact, a rough extrapolation of the growth curves to the total luminosity $L_{200}$ within $R_{200}$ shows that for the poorest clusters $L_{200}$ is roughly 1.7 times the luminosity within 500 kpc, whereas for the richest clusters $L_{200}$ is roughly 2.5 times this luminosity. This particularly affects the light fraction contributed by the BCG: although in the fixed 500-kpc aperture the BCG represents an almost constant fraction of the total light, independent of the cluster richness, the same fraction within $R_{200}$ would show a decreasing trend with richness, as found by Lin & Mohr (2004).

The analysis of the colour profiles in Fig. 5(d) demonstrates that the ICL colours are consistent with (in $g - r$) or marginally redder than (in $r - i$) the average colours of galaxies. This result is compatible with the idea that the ICL originates from stripped stars and disrupted galaxies. Given the relatively large uncertainties in our colour estimates, we cannot test the slightly different predictions obtained by the recent $N$-body+SPH simulations of Murante et al. (2004), Sommer-Larsen et al. (2005) and Willman et al. (2004). In fact, they all agree in predicting that intracluster stars must have roughly the same colours and metallicities as the dominant stellar population in galaxies, but while Murante et al. (2004) and Sommer-Larsen et al. (2005) predict slightly larger ages for the intracluster stars, Willman et al. (2004) argue that the typical intracluster stellar population should be similar to those in intermediate luminosity galaxies.

As a final remark, we note that in a scenario where the ICL originates from stripping and galaxy disruption, the galaxies that contribute most of the ICL are those plunging into the cluster potential along nearly radial orbits (e.g. Moore et al. 1996), with some of them eventually merging into the BCG. If there is a significant anisotropy in the orientation of the orbits, a significant elongation in the shape of the BCG and of the ICL should be observable. However, because of the shorter orbital and scattering times at higher densities, the elongation is expected to increase with increasing

clustercentric distances, up to the asymptotic value given by the 'original' distribution of orbital parameters. This may explain the outwardly increasing ellipticities of the ICL isophotes which we found above (see Fig. 6).

## 8 CONCLUSIONS

In this paper we have studied the mean properties of the intracluster optical emission of 683 clusters of galaxies between $z = 0.2$ and 0.3, imaged by the SDSS. Thanks to the high sensitivity achieved by stacking the imaging data, we have been able to trace the average SB profile of the ICL out to 600–700 kpc from the BCG. The measured SB ranges from 27.5 mag arcsec$^{-2}$ at 100 kpc to $\sim$32 mag arcsec$^{-2}$ at 700 kpc in the observed $r$-band, which corresponds to a $\sim$1 mag arcsec$^{-2}$ brighter rest-frame $g$-band SB. The ICL fraction depends at most weakly on global cluster properties, such as BCG luminosity and richness. The ICL is ubiquitous in clusters of galaxies, as demonstrated by significant detections in all our subsamples.

We find that the ICL contributes in the mean 30–40 per cent of the total optical emission at around 100 kpc and a decreasing fraction at larger clustercentric distance, down to <5 per cent at 600–700 kpc. By integrating the fluxes of the different components within 500 kpc we obtain $10.9 \pm 1.0$ per cent for the fraction of light in the ICL and $21.9 \pm 1.0$ per cent for the BCG. Taking sampling uncertainties and systematic errors into account, the total errors on these fractions are about $\pm 5$ per cent for the ICL and $\pm 3$ per cent for the BCG. Our measurements of the diffuse light also put an independent constraint on the shape of the cluster luminosity function: faint-end slopes $\alpha < -1.35$ are rejected as inconsistent.

The higher spatial concentration of the ICL with respect to the starlight in galaxies indicates that the production mechanism for the ICL is more efficient the deeper one goes into the cluster potential well. Comparing different subsamples of clusters, we have observed a significant correlation of the surface brightness of the ICL with the luminosity of the BCG, as well as with the richness of the cluster, suggesting a link between the mechanisms responsible for the growth of the BCG and for the accumulation of intracluster stars.

The similarity in colours between the ICL and galaxies supports a scenario where intracluster stars originate in galaxies and are subsequently dispersed in the intracluster space by dynamical interactions leading to galaxy stripping or disruption. Moreover, the analysis of the shape (ellipticity) of the ICL with respect to the BCG core suggests that the main mechanism acting to create the ICL is the tidal interaction of galaxies with the central cluster potential. This would also explain the observed link between the amount of ICL and the luminosity of the BCG, the latter being strongly correlated to the depth of the potential well.

Due to the very large sample size and to the unprecedented depth of the present observations, our results provide the best and statistically most representative measurement of the intracluster light so far over a wide range of cluster types. Future extensions of our sample to the entire SDSS area and to nearer clusters, and improvements in classification algorithms for galaxy clusters, will not only improve the sensitivity of our measurements, but also make it possible to study the relationship between cluster properties and the ICL in greater detail, providing new clues and stronger constraints on dynamical processes during the formation and evolution of galaxy clusters.

## ACKNOWLEDGMENTS

We thank Jim Annis for kindly providing us with the maxBCG catalogue of clusters used in this work, and Sarah Hansen for making available unpublished results on the photometric determination of $R_{200}$. Thanks to the referee Neil Trentham for comments that have significantly improved this paper, to Anthony Gonzalez and Magda Arnaboldi for very stimulating discussions and the fruitful comparisons of respective results, and to Anna Gallazzi for her precious help.

This paper is dedicated to Jatush Sheth.

Funding for the creation and distribution of the SDSS Archive has been provided by the Alfred P. Sloan Foundation, the Participating Institutions, the National Aeronautics and Space Administration, the National Science Foundation, the US Department of Energy, the Japanese Monbukagakusho, and the Max Planck Society. The SDSS Web site is http://www.sdss.org/.

The SDSS is managed by the Astrophysical Research Consortium (ARC) for the Participating Institutions. The Participating Institutions are The University of Chicago, Fermilab, the Institute for Advanced Study, the Japan Participation Group, The Johns Hopkins University, the Korean Scientist Group, Los Alamos National Laboratory, the Max-Planck-Institute for Astronomy (MPIA), the Max-Planck-Institute for Astrophysics (MPA), New Mexico State University, University of Pittsburgh, Princeton University, the United States Naval Observatory, and the University of Washington.

## REFERENCES

Abazajian K., et al., 2003, AJ, 126, 2081
Abazajian K. et al., 2004, AJ, 128, 502
Abell G. O., 1958, ApJS, 3, 211
Abell G. O., Corwin H. G., Olowin R. P., 1989, ApJS, 70, 1
Arnaboldi M. et al., 1996, ApJ, 472, 145
Bahcall N. A. et al., 2003, ApJS, 148, 243
Bartelmann M., 1996, A&A, 313, 697
Bernstein G. M., Nichol R. C., Tyson J. A., Ulmer M. P., Wittman D., 1995, AJ, 110, 1507
Bertin E., Arnouts S., 1996, A&AS, 117, 393
Binggeli B., 1982, A&A, 107, 338
Binggeli B., Sandage A., Tammann G. A., 1985, AJ, 90, 1681
Blanton M. R., Lin H., Lupton R. H., Maley F. M., Young N., Zehavi I., Loveday J., 2003a, AJ, 125, 2276
Blanton M. R. et al., 2003b, ApJ, 594, 186
Bruzual G., Charlot S., 2003, MNRAS, 344, 1000
Calcáneo-Roldán C., Moore B., Bland-Hawthorn J., Malin D., Sadler E. M., 2000, MNRAS, 314, 324
Carlberg R. G. et al., 1997, ApJ, 485, L13
de Vaucouleurs G., 1948, Annales d'Astrophysique, 11, 247
Dressler A., 1979, ApJ, 231, 659
Durrell P. R., Ciardullo R., Feldmeier J. J., Jacoby G. H., Sigurdsson S., 2002, ApJ, 570, 119
Eisenstein D. J. et al., 2001, AJ, 122, 2267
Feldmeier J. J., Ciardullo R., Jacoby G. H., Durrell P. R., Mihos J. C., 2004a, in Duc P.-A., Braine J., Brinks, E., eds, IAU Symp. 217, Intracluster Planetary Nebulae in Clusters and Groups. Astron. Soc. Pac., San Francisco, p. 86
Feldmeier J. J., Mihos J. C., Morrison H. L., Harding P., Kaib N., Dubinski J., 2004b, ApJ, 609, 617
Feldmeier J. J., Ciardullo R., Jacoby G. H., Durrell P. R., 2004c, ApJ, 615, 196
Feldmeier J. J., Mihos J. C., Morrison H. L., Rodney S. A., Harding P., 2002, ApJ, 575, 779
Fukugita M., Ichikawa T., Gunn J. E., Doi M., Shimasaku K., Schneider D. P., 1996, AJ, 111, 1748
Gnedin O. Y., 2003, ApJ, 589, 752
Gonzalez A. H., Zabludoff A. I., Zaritsky D., 2005, ApJ, 618, 195
Gonzalez A. H., Zabludoff A. I., Zaritsky D., Dalcanton J. J., 2000, ApJ, 536, 561

© 2005 RAS, MNRAS **358**, 949–967

Goto T. et al., 2002, PASJ, 54, 515
Gregg M. D., West M. J., 1998, Nat, 396, 549
Gunn J. E. et al., 1998, AJ, 116, 3040
Hansen S. M., McKay T. A., Annis J., Kimball A., Sheldon E. S., Wechsler R. H., 2002, BAAS, 34, 1167
Hansen S. M., McKay T. A., Wechsler R. H., Annis J., Sheldon E. S., Kimball A., 2005, ApJ, submitted
Hogg D. W., Finkbeiner D. P., Schlegel D. J., Gunn J. E., 2001, AJ, 122, 2129
Ivezić Ž. et al., 2002, in Green R. F., Khachikian E. Ye., Sanders D. B., eds, ASP Conf. Ser. Vol. 284, AGN Surveys. Astron. Soc. Pac., San Francisco, p. 137
Jedrzejewski R. I., 1987, MNRAS, 226, 747
Lambas D. G., Maddox S. J., Loveday J., 1992, MNRAS, 258, 404
Lin Y., Mohr J. J., 2004, ApJ, 617, 879
Lupton R. H., Gunn J. E., Ivezić Z., Knapp G. R., Kent S., Yasuda N., 2001, in Harnden F. R., Jr, Primini F. A., Payne H. E., eds, ASP Conf. Ser. Vol. 238, Astronomical Data Analysis Software and Systems X. Astron. Soc. Pac., San Francisco, p. 269
Melnick J., Hoessel J., White S. D. M., 1977, MNRAS, 180, 207
Merritt D., 1984, ApJ, 276, 26
Mihos J. C., 2004, in Duc P.-A., Braine J., Brinks, E., eds, IAU Symp. 217, Intracluster Planetary Nebulae in Clusters and Groups. Astron. Soc. Pac., San Francisco, p. 390
Mobasher B. et al., 2003, ApJ, 587, 605
Moore B., Katz N., Lake G., Dressler A., Oemler A., 1996, Nat, 379, 613
Murante G. et al., 2004, ApJ, 607, L83
Napolitano N. R. et al., 2003, ApJ, 594, 172

Navarro J. F., Frenk C. S., White S. D. M., 1995, MNRAS, 275, 720
Pier J. R., Munn J. A., Hindsley R. B., Hennessy G. S., Kent S. M., Lupton R. H., Ivezić Ž., 2003, AJ, 125, 1559
Porter A. C., Schneider D. P., Hoessel J. G., 1991, AJ, 101, 1561
Press W. H., Teukolsky S. A., Vetterling W. T., Flannery B. P., 1992, Numerical Recipes in C. The Art of Scientific Ccomputing. Cambridge Univ. Press, Cambridge
Richstone D. O., 1976, ApJ, 204, 642
Sabatini S., Davies J., Scaramella R., Smith R., Baes M., Linder S. M., Roberts S., Testa V., 2003, MNRAS, 341, 981
Schlegel D. J., Finkbeiner D. P., Davis M., 1998, ApJ, 500, 525
Schombert J. M., 1986, ApJS, 60, 603
Schombert J. M., 1988, ApJ, 328, 475
Smith J. A. et al., 2002, AJ, 123, 2121
Sommer-Larsen J., Romeo A. D., Portinari L., 2005, MNRAS, 357, 478
Stoughton C. et al., 2002, AJ, 123, 485
Strauss M. A. et al., 2002, AJ, 124, 1810
Trentham N., Hodgkin S., 2002, MNRAS, 333, 423
Trentham N., Mobasher B., 1998, MNRAS, 293, 53
Welch G. A., Sastry G. N., 1971, ApJ, 169, L3
Willman B., Governato F., Wadsley J., Quinn T., 2004, MNRAS, 355, 159
York D. G. et al., 2000, AJ, 120, 1579
Zibetti S., White S. D. M., Brinkmann J., 2004, MNRAS, 347, 556
Zwicky F., 1951, PASP, 63, 61

This paper has been typeset from a TEX/LATEX file prepared by the author.